

## RESEARCH ARTICLE

10.1002/2017JA024414

## Key Points:

- The first in situ observations of suprathermal  $\text{Fe}^+$  in and near Earth's magnetosphere are reported using 21 years of Geotail data
- A rare species,  $\text{Fe}^+$  occurrence is positively associated with both geomagnetic ( $Kp$ ) and solar ( $F_{10.7}$ ) activity indices
- $\text{Fe}^+$  of likely ionospheric origin dominates at  $Kp < \sim 4$ ; at  $Kp > \sim 4$ , solar wind and/or inner source-derived  $\text{Fe}^+$  may contribute

## Supporting Information:

- Supporting Information S1

## Correspondence to:

S. P. Christon,  
spchriston@aol.com

## Citation:

Christon, S. P., Hamilton, D. C., Plane, J. M. C., Mitchell, D. G., Grebowsky, J. M., Spjeldvik, W. N., & Nylund, S. R. (2017). Discovery of suprathermal ionospheric origin  $\text{Fe}^+$  in and near Earth's magnetosphere. *Journal of Geophysical Research: Space Physics*, 122, 11,175–11,200. <https://doi.org/10.1002/2017JA024414>

Received 30 MAY 2017

Accepted 27 AUG 2017

Accepted article online 31 AUG 2017

Published online 14 NOV 2017

©2017. American Geophysical Union.  
All Rights Reserved.

## Discovery of Suprathermal Ionospheric Origin $\text{Fe}^+$ in and Near Earth's Magnetosphere

S. P. Christon<sup>1</sup> , D. C. Hamilton<sup>2</sup> , J. M. C. Plane<sup>3</sup> , D. G. Mitchell<sup>4</sup> , J. M. Grebowsky<sup>5</sup> ,  
W. N. Spjeldvik<sup>6</sup> , and S. R. Nylund<sup>4</sup> 

<sup>1</sup>Focused Analysis and Research, Columbia, MD, USA, <sup>2</sup>Department of Physics, University of Maryland, College Park, MD, USA, <sup>3</sup>School of Chemistry, University of Leeds, Leeds, UK, <sup>4</sup>The Johns Hopkins University Applied Physics Laboratory, Laurel, MD, USA, <sup>5</sup>NASA Goddard Space Flight Center, Greenbelt, MD, USA, <sup>6</sup>Department of Physics, Weber State University, Ogden, UT, USA

**Abstract** Suprathermal (87–212 keV/e) singly charged iron,  $\text{Fe}^+$ , has been discovered in and near Earth's  $\sim 9\text{--}30 R_E$  equatorial magnetosphere using  $\sim 21$  years of Geotail STICS (suprathermal ion composition spectrometer) data. Its detection is enhanced during higher geomagnetic and solar activity levels.  $\text{Fe}^+$ , rare compared to dominant suprathermal solar wind and ionospheric origin heavy ions, might derive from one or all three candidate lower-energy sources: (a) ionospheric outflow of  $\text{Fe}^+$  escaped from ion layers near  $\sim 100$  km altitude, (b) charge exchange of nominal solar wind iron,  $\text{Fe}^{+2}$ , in Earth's exosphere, or (c) inner source pickup  $\text{Fe}^+$  carried by the solar wind, likely formed by solar wind Fe interaction with near-Sun interplanetary dust particles. Earth's semipermanent ionospheric  $\text{Fe}^+$  layers derive from tons of interplanetary dust particles entering Earth's atmosphere daily, and  $\text{Fe}^+$  scattered from these layers is observed up to  $\sim 1000$  km altitude, likely escaping in strong ionospheric outflows. Using  $\sim 26\%$  of STICS's magnetosphere-dominated data when possible  $\text{Fe}^{+2}$  ions are not masked by other ions, we demonstrate that solar wind Fe charge exchange secondaries are not an obvious  $\text{Fe}^+$  source. Contemporaneous Earth flyby and cruise data from charge-energy-mass spectrometer on the Cassini spacecraft, a functionally identical instrument, show that inner source pickup  $\text{Fe}^+$  is likely not important at suprathermal energies. Consequently, we suggest that ionospheric  $\text{Fe}^+$  constitutes at least a significant portion of Earth's suprathermal  $\text{Fe}^+$ , comparable to the situation at Saturn where suprathermal  $\text{Fe}^+$  is also likely of ionospheric origin.

### 1. Introduction

The presence of suprathermal ( $\sim 83\text{--}167$  keV/e), ionospheric origin singly charged iron,  $\text{Fe}^+$  in Saturn's magnetosphere was by Christon et al. (2015) documented and established using the CHEMS “charge-energy-mass ion spectrometer” on the Cassini spacecraft (Krimigis et al., 2004). Using the years 2000 to 2008 from the present data set, the discovery of  $\text{Fe}^+$  in the  $\sim 9 \times 30 R_E$  region near Earth was reported by Christon, Hamilton, Mitchell, Plane, et al. (2014). The  $\sim 21$  year, 1995-060 to 2015-365 (year-day of year), long-term data set analyzed here are, to our knowledge, the first to reveal suprathermal  $\text{Fe}^+$  and Earth's molecular ions, herein called  $\text{MI}^+$ , up to  $\sim 5\text{--}15 R_E$  sunward of the bow shock apex in the upstream foreshock region. ( $\text{MI}^+$ , the triad of 28–32 amu/e molecular ions,  $\text{N}_2^+$ ,  $\text{NO}^+$ , and  $\text{O}_2^+$ , are discussed in a companion publication.) We present observational evidence of suprathermal  $\text{Fe}^+$  at  $\sim 87\text{--}212$  keV/e in and near Earth's magnetosphere using the STICS (suprathermal ion composition spectrometer) instrument on the Geotail spacecraft (Williams et al., 1994), which is functionally identical to the CHEMS instrument used at Saturn.

At Earth both ionospheric origin ions and solar wind ions have relatively easy access to Earth's magnetosphere by either escaping from an internal source, the ionosphere, or entry from an external source, the solar wind, respectively. Both ion populations mix and can subsequently escape Earth's environs after being transformed in both energy and/or charge state by particle scattering, magnetospheric processes, magnetopause reconnection, and magnetosheath turbulence. For example, low-charge-state (LCS) suprathermal ionospheric  $\text{O}^+$  and  $\text{N}^+$  have been observed from just upstream of the bow shock (Christon et al., 2000; Keika et al., 2004) up to  $\sim 100 R_E$  near L1 (Posner et al., 2002). Ionospheric  $\text{N}^+$ ,  $\text{O}^+$ , and  $\text{MI}^+$  were observed flowing antisunward at  $\sim 146 R_E$  downtail at the time of a concurrent geomagnetic activity enhancement (Christon, Gloeckler, et al., 1994). On the other hand, the nominal high-charge-state (HCS) solar wind ions swC, swN, swO, and swFe (primarily  $\text{Fe}^{+7\text{--}14}$ ) are often observed in the near-Earth magnetosphere (Christon, Hamilton, et al., 1994), similar to that typically observed in the solar wind (see Figure 2a) (Bame, 1972;

von Steiger et al., 2000). Please note that (1) when referencing a multiply charged ion species  $M$  herein,  $M^{+a:+b}$ , the trailing superscript textual construct  $+a:+b$  denotes the ion charge  $Q$  states  $+a < Q < +b$  and (2), for clarity, we (a) call the Sun's ions in the solar wind plasma originating at the Sun either "core solar wind ions" or solar wind "primaries," and their charge exchange products from interactions in Earth's magnetosphere solar wind "secondaries," and (b) occasionally use the prefixes "sw" and "io" to denote solar wind and ionosphere origin, respectively. Core solar wind ion energies are in the range  $\sim 0.3\text{--}5$  keV/amu, while the solar wind suprathermal tail extends from  $\sim 8$  keV/amu upward (see, e.g., Figures 1 and 2 in Mewaldt et al. (2001) and their discussion). O and N can originate in both the solar wind (at high and low charge states from core solar wind and from pickup ions, respectively) and in the ionosphere (at low charge states). In order to clarify our discussion of particles from different sources at times, as done above, we designate the high-charge-state, high-mass core solar wind ions such as  $C^+$ ,  $O^+$ , and  $Fe^+$  ions as "swC<sup>+</sup>," "swO<sup>+</sup>," and "swFe<sup>+</sup>," respectively. Ions picked-up by the solar wind are designated as puC<sup>+</sup>, puO<sup>+</sup>, puNe<sup>+</sup>, etc. Additionally, we designate ionospheric origin ions  $O^+$ ,  $N^+$ , and  $Fe^+$  as ioO<sup>+</sup>, ioN<sup>+</sup>, and ioFe<sup>+</sup>, to separate their discussion from that of HCS solar wind ions. A glossary (section 6) lists often used acronyms.

Below, we briefly review observations of solar wind, ionospheric, inner source, and other less likely higher-energy ion populations relevant to this  $Fe^+$  analysis.

### 1.1. Suprathermal Solar Wind Ions

Suprathermal high-energy solar wind ions extend above  $\sim 8$  keV/amu in interplanetary space (see, e.g., Gloeckler, 2003; Gloeckler et al., 1992, Figure 13; Mewaldt et al., 2001). Christon, Hamilton, et al. (1994) measured suprathermal tails of swC and swO primaries and secondaries at  $7\text{--}9 R_E$  energized up to  $\sim 300$  keV/e in Earth's nightside magnetosphere. For clarity,  $\sim 10$  keV/amu  $Fe^{+7}$  may equally be referred to as  $\sim 560$  keV  $Fe^{+7}$  or  $\sim 80$  keV/e  $Fe^{+7}$  and is in the range of Fe addressed in this study; however, we most often use the natural energy measurement of the instrument  $E/Q$ , total energy per charge, and keV/e, for convenience. Over a sufficient amount of time after entering Earth's magnetosphere, the HCS solar wind ions charge exchange predominantly to lower charge states with near-Earth particles (Christon, Hamilton, et al., 1994; Spjeldvik, 1979; Spjeldvik et al., 2002).

Dominant HCS swFe primaries in nominal equatorial coronal hole flow, nominally with charge states  $Fe^{+7:+14}$  (Lepri & Zurbuchen, 2010; Lepri et al., 2001), are commonly observed in the near-Earth magnetosphere (see Christon, Hamilton, et al. (1994) and Figure S3 in the supporting information) and have been reported and modeled in the inner magnetosphere (Gloeckler et al., 1985; Gloeckler & Hamilton, 1987; Spjeldvik et al., 2002) and low Earth orbit (Mazur et al., 1999). The ratio  $Fe^{+6}/Fe^{+7}$  in the nominal core solar wind flow is found to be  $\sim 0.003$  to  $\sim 0.005$  (Heidrich-Meisner et al., 2016; Lepri et al., 2001), although very rare lower swFe charge states ( $Fe^{+3:+5}$ ) can be present (Geiss et al., 1992). Lepri and Zurbuchen (2010) present samples of cold solar coronal mass ejections (CMEs) with  $Fe^{+4}$  (see also Geiss et al., 1992); CMEs typically contain very high charge state Fe, such as  $Fe^{+8:+24}$  (Lepri et al., 2001). Notably, Gilbert et al. (2012) inspect eight infrequently observed cold CMEs containing rare embedded solar filament material (Lepri & Zurbuchen, 2010); Gilbert et al. (2012), whose instrumentation could not resolve  $Fe^{+1}$ , report core swFe charge state distributions that extend to and can include  $Fe^{+2}$  (note their Figure 2b). Further, Klecker et al., (2009), in the first study comparing the measured Fe charge states in lower-energy core solar wind to its suprathermal tail, found that the suprathermal tails typically have higher mean ionic charge states. In a sample presented by Klecker et al. (2009) (with overall daily mean charge state distributions ranging from  $Q \sim 5$  to  $Q \geq 20$ ), core swFe is approximately bimodal, favoring  $\sim 5 \leq Q \leq \sim 13$  charge states, and the simultaneously measured solar wind suprathermal tails ( $10\text{--}100$  keV/amu or  $35\text{--}350$  keV/e at  $Q = 16$ ) are clearly dominated by a single peak at  $Q > 14$  charge states. Klecker et al. (2009) state that "this appears to suggest a somewhat increased injection and acceleration of Fe ions with the higher charge states from the solar wind into the suprathermal ion distribution." Therefore, the instruments used in this study are likely not able to identify the core-energy solar-filament low-charge-state solar wind ions noted above. However, if solar-filament swFe charge states enter the magnetosphere and are accelerated, our instrument should be able to detect the  $Fe^{+2}$  ions.

$Fe^+$  derived from HCS swFe charge exchange secondaries in Earth's magnetosphere, a transformation from  $Q \geq +6$  down to  $Q = +1$ , should be possible given that heavy solar wind ions appear to have relatively easy entrance access to the magnetosphere and adequate time to interact repeatedly with Earth's exosphere

(Christon, Hamilton, et al., 1994; Spjeldvik et al., 2002). Conversely, at Saturn, with an even larger and stronger magnetosphere, we show below that relative to solar wind HCS heavy ions (C, O, and Mg-Si-S) which are clearly present in Saturn's magnetosphere, only a trace of solar wind Fe (swFe) primaries was possibly detected inside Saturn's magnetosphere. Consequently, no swFe charge exchange products were observed in Saturn's equatorial plasma sheet region, leading Christon et al. (2015) to conclude that Saturn's  $\text{Fe}^+$  was most likely produced internally, probably from ionospheric outflow.

## 1.2. Outflowing Ionospheric Ions

The outflow of metal ions,  $\text{Fe}^+$ , in particular, from Earth's ionosphere is a highly likely process, although it is not yet recognized or documented, likely for lack of detailed, modern heavy ion composition observations in relevant portions of Earth's thermosphere, ionosphere, and exosphere. Metal atom and ion layers are a well-documented and understood feature of Earth's thermosphere and lower ionosphere. Incoming interplanetary dust particles (IDPs) readily produce layers of metal atoms ions in the lower ionosphere, specifically Fe and  $\text{Fe}^{+1}$  herein (Plane, 2012; Plane et al., 2015). Ionospheric metal layers, observed in situ at Earth (Grebowsky & Aikin, 2002) and Mars (Grebowsky et al., 2017) are also remotely detected at some and expected at most planets in our solar system (Grebowsky et al., 2002; Molina-Cuberos et al., 2008) except possibly at Mercury, whose tenuous and variable atmosphere/exosphere probably lacks sufficient density and structure to support even sporadic layers in spite of its strong intrinsic dipole magnetic field. Isolated metal layers at Mars, which has patches of remanent planetary magnetic field (Andrews et al., 2015), mimic Earth's sporadic metal *E* layers (Grebowsky et al., 2017), demonstrating the ubiquity of this process. At Earth, around 80% (by mass) of the metal layer's particles originate from small interplanetary debris particles produced by sublimation of short-period Jupiter family comets, and the rest from asteroidal collisions and long-period comets and asteroids (Carrillo-Sánchez et al., 2015; Plane et al., 2015; Rubin & Grossman, 2010). The metal atom layers are determined to have a mean residence time of  $\sim 4.3$  years in Earth's atmosphere before planetary deposition (Dhomse et al., 2013). The ablation of IDPs injects a variety of metals (mainly Na, Mg, Si, K, Ca, and Fe) into Earth's upper mesosphere and lower thermosphere, giving rise to layers of metal atoms and ions typically between  $\sim 80$  and 110 km altitude, although recent observations of Fe atom layers at 110–155 km altitudes above Antarctica (Chu et al., 2011; Plane et al., 2015) suggest that all is not yet known about the thermosphere/ionosphere metal layers. The ion peaks are nominally found  $\sim 5$ –10 km above the atom peaks, where the heavier Fe layers are  $\sim 4$  km below the other metal layers (Dawkins et al., 2016; Plane et al., 2015). The metal ions are produced both by hyperthermal collisions with air molecules immediately following ablation and also by charge transfer between Fe and the ambient *E* region ions  $\text{NO}^+$  and  $\text{O}_2^+$ . Low concentrations of metal ions are found at altitudes higher than the main metal ion layers and extend well above the peak  $\text{O}^+$  density of the *F* layer at  $\sim 200$ –300 km. The metal atom and ion layers range from dayside to nightside local times, and at latitudes from Earth's equator to poleward of the auroral regions (Chu et al., 2011; Grebowsky & Aikin, 2002; Plane et al., 2015).  $\text{Fe}^+$  was detected at altitudes of 408 to 936 km, from  $-14.3^\circ$  to  $+16^\circ$  geomagnetic latitude, by Hanson et al. (1972). Kumar and Hanson (1980) find a strong positive correlation between solar activity and metal ion ( $\text{Fe}^+$  and  $\text{Mg}^+$ ) detection probability at low latitudes ( $\leq 35^\circ$ ) and high altitudes ( $\sim 700$ –1000 km) at night, with statistically significant detection probabilities ranging from  $\sim 0.1\%$  to 0.8% (mean  $\sim 0.4\%$ ). A discussion of the various ion energization mechanisms in the thermosphere/ionosphere is beyond the scope of this work, but an extended discussion of mechanisms relevant to  $\text{O}^+$  and molecular ions,  $\text{MI}^+$ , can be found in Peterson et al. (1994). Of note is that the escape velocity of  $\text{Fe}^+$  is less than twice the escape velocity of  $\text{O}_2^+$ .

At middle to low latitudes the  $\text{Fe}^+$  ions are possibly driven upward by electrodynamic processes driven by the neutral winds (Carter & Forbes, 1999; Thayer, 1998), combined with the fountain effect (Lockwood et al., 1985). Sufficient energization for  $\text{Fe}^+$  to escape into the magnetosphere is likely associated with the dayside cusp and/or nightside auroral regions at high latitudes where strong upflow of ions to altitudes far above the ionospheric metal layers would be related to local electrodynamics, wave activity, and associated geomagnetic disturbance. Most low-/middle-latitude metal ions may never reach the cusp and auroral regions but those that do will participate in the extant processes. To our knowledge there is presently no envisioned single escape process that can transport the thermal metal layer ion component from low altitudes into the magnetosphere while energizing them to tens of keV. Most scenarios incorporate a multistep procedure, even for  $\text{O}^+$ , much less  $\text{MI}^+$ . Such a discussion is beyond the scope of this study, and detailed composition and

velocity distribution at numerous altitudes is lacking. Metal layers at other planets are formed by the same universal processes (Benna et al., 2015; Grebowsky & Aikin, 2008; Pesnell & Grebowsky, 2001).

### 1.3. Inner Source Pickup Ions

The currently most consistent explanation of inner source pickup ions involves solar wind interaction with IDPs that fall toward the Sun; just as IDPs fall toward Earth and into its atmosphere, IPDs are drawn toward the Sun and ablate in the process (see Berger et al., 2015; Wimmer-Schweingruber & Bochsler, 2003). Dust grains are a product of the near-Sun-ablated IDPs. Solar wind ions can pass through those grains with a thickness comparable to the solar wind ion penetration depth; that is, just as ions pass through our instruments' carbon foil) and lose all or most of their initial charge, those interacting solar wind ions exit the dust nanograins with  $Q = 0$  or  $\pm 1$  (Allegrini et al., 2005; Berger et al., 2015; Mann & Czechowski, 2005; Taut et al., 2015; Wimmer-Schweingruber & Bochsler, 2003). The now low-charge-state solar wind ions are picked-up by the solar wind, escaping the Sun with the solar wind. These ions form a unique low-energy ion population in the heliosphere known as the inner source pickup ions (ISPUI). The above source description explains much of the elemental composition similarities of core solar wind ions and ISPUI, allows for extant composition differences, and provides mechanisms for converting core HCS solar wind ions into singly charged cooler pickup ions. ISPUI are observed at high and low latitudes throughout the heliocentric distance range traveled by the Ulysses spacecraft, 1.35–5.4 AU, in slow and fast solar wind (Gloeckler et al., 2010; Gloeckler & Geiss, 1998). Measured and identified ISPUI heavy ion composition is  $C^+$ ,  $N^+$ ,  $O^+$ ,  $Ne^+$ ,  $Na^+$ ,  $Mg^+$ ,  $Ar^+$ ,  $Sr^+$ ,  $Kr^+$ ,  $Al^+$  (and/or  $Fe^{+2}$ ) and various molecular ion species (Gloeckler & Geiss, 2001; Gloeckler, Fisk, Geiss et al., 2000; Gloeckler, Fisk, Zurbuchen et al., 2000; Gloeckler et al., 2010; Geiss et al., 1995; Taut et al., 2015), with  $puC^+$  and  $puO^+$  being the primary heavy ion components with comparable intensities (to within ~50% depending on the sample; see Gloeckler, Fisk, Geiss, et al. (2000, 2010) and Table S10 in the supporting information). Gloeckler et al. (2010) analyze ~6.2 years of Ulysses ISPUI  $10 \leq M/Q \leq 57$  amu/e ion data. As a result of poor statistics above  $M/Q \sim 25$  amu/e, all ion species are not identified in their Figure 4 and Table 1; six peaks are fit with curves but unlabeled. The highest- $M/Q$ -labeled peak is  $SO^+$  at ~49 amu/e (molecular ions in this type of instrument typically register a slightly higher  $M/Q$  than the intended species'  $M/Q$ ) (see e.g., Christon et al., 2013). A distinct, isolated peak that was fit in Gloeckler et al. (2010) but not labeled and is present at ~56 amu/e, having ~43% of the counts of  $SO^+$ . It is not the smallest peak that they fit with a curve. Although not labeled as  $Fe^+$ , in their Figure 4, Gloeckler et al. (2010) drew a lognormal gaussian curve fit to it, suggesting that this unlabeled peak might have been treated as  $Fe^+$  (see the footnote 1 on page 516 of Gloeckler et al. (2010)). We take that small peak at ~56 amu/e as representing an upper limit on ISPUI  $Fe^+$ . It is the only quantitative measure of ISPUI  $Fe^+$  we found in the literature, all other references to ISPUI  $Fe^+$  that we have reviewed are made without the presentation of ISPUI  $Fe^+$  observations. We visually fit the Gloeckler et al. (2010) count/bin peaks for  $O^+$  and  $C^+$ , as well as the possible  $Fe^+$  peak graphically with an exponential functional form and determine the upper limit ISPUI count ratio,  $Fe^+/C^+_{ISPUI}$ , to be  $0.005 \pm 0.005$  (see Table S10 in the supporting information). The  $puC^+$  count rate drops off with heliocentric radial distance  $R_H$  as  $R_H^{-1.53}$ , peaking at midlatitudes and dropping to its lowest values in the ecliptic plane (Gloeckler et al., 2010). In this paper we do not address the inner source light ions  $puH^+$ ,  $puHe^+$ , and  $puHe^{+2}$ , focusing solely on  $O^+$ ,  $C^+$ , and  $Fe^+$ . Gloeckler, Fisk, Geiss, et al. (2000) found the core solar wind as the most likely source of the inner source ions, compared to corotating interaction region (CIR) ions. Schwadron et al. (2002) suggested that  $Fe^+$  ( $M/Q = 56$  amu/e) might be an ISPUI component. With C and O being the dominant heavy elements in both populations, von Steiger et al. (2000) find an average core solar wind elemental ratio  $C/O_{SW} \sim 0.68$  and Gloeckler et al. (2010) find an inner source elemental ratio  $C/O_{ISPUI} \sim 0.51$  (their Table 1), so there are important solar wind and ISPUI species abundance differences (see Table S10 in the supporting information) which likely depend on ISPUI production processes at the IDPs in the near-Sun region. The ISPUI are different from what we herein call the outer source pickup ions (OSPUI), which are derived from (1) interstellar pickup ions generated from the passage and ionization of interstellar gas interacting with the Sun on its way through the solar system and (2) the LCS ions created by the proposed interaction between the solar wind and interstellar dust from the Edgeworth-Kuiper Belt at 10–50 AU (Gloeckler & Geiss, 1998; Kallenbach et al., 2000; Möbius et al., 1985). First identified with  $He^+$  near Earth, OSPUI are composed of  $H^+$ ,  $He^+$ ,  $He^{+2}$ ,  $N^+$ ,  $O^+$ , and  $Ne^+$  (Gloeckler & Geiss, 1998). OSPUI  $He^+$  has maximum flux near ~1 AU peaked in a focusing cone in the direction opposite to the incoming interstellar wind, with decreasing flux extending back to the Sun and out to the heliopause (Gloeckler et al., 2004). OSPUI  $O^+$

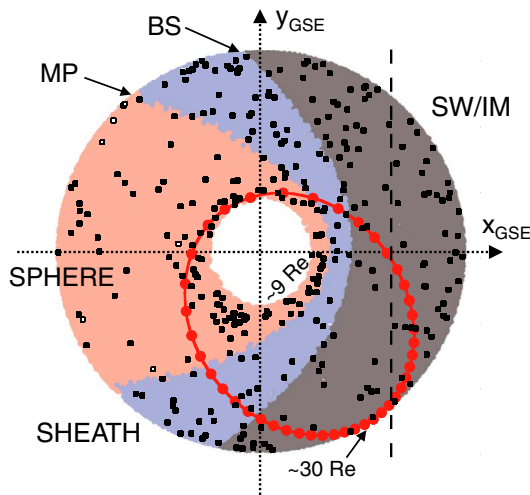


**Figure 1.** Plasma regimes assigned to Geotail’s near-Earth location in geocentric solar ecliptic coordinates from early 1995 to 2015 are color coded (see text); 3 h points along one  $\sim 9 \times 30 R_E$  orbit are shown. The SPHERE, the primary plasma regime inside the magnetopause, contains the plasma sheet, ring current, and near-Earth locations, excludes magnetospheric boundary layers and the LOBE (not shown, but roughly colocated with and lying above and below the SPHERE layer). SHEATH locations are outside the magnetopause and inside the bow shock, the earthward boundary of the solar wind/interplanetary medium, SW/IM. The long dashed line at  $X_{GSE} \sim 20 R_E$  is the near-Earth bound of a strict SW/IM selection. Small symbols are locations of the  $Fe^+$  observations (open symbols for the LOBE and closed dots for other regions).

number density, which is comparable to that of ISPU  $O^+$  near  $\sim 1$  AU, increases out to  $\geq 5$  AU, whereas the ISPU  $O^+$  density increases toward the Sun (Gloeckler & Geiss, 1998). The ISPU source produces ions observed at all distances out to at least  $\sim 5$  AU and all latitudes (Gloeckler & Geiss, 1998). Given the lack of specific quantification of ISPU  $Fe^+$  in the literature, barring the above documented possible observation by Gloeckler et al. (2010), we treat our derived estimates of ISPU  $Fe^+$  and  $Fe^+/C_{ISPU}^+ = 0.005 \pm 0.005$  as unverified upper limits.

**1.4. Other Possible Suprathermal Ion Sources**

Finally, solar flare ejections contain HCS  $Fe$  ions, mostly  $Fe^{+10:+20}$ , with suprathermal high-energy tails up to  $\sim 180\text{--}540$  keV/nucleon (Gloeckler, 2003; Mewaldt et al., 2001; Möbius et al., 1999). CIR ion populations also have an overall heavy ion elemental composition comparable to the solar wind (see Table 1 of Gloeckler, Fisk, Geiss, et al. (2000) and Table S10 in the supporting information). Both ion groups enter Earth’s magnetosphere with the solar wind (Fujimoto et al., 1998; Terasawa et al., 1997) and their  $Fe$  charge exchanges with near-Earth particles down to lower  $Fe$  charge states. Equilibrium calculations for keV to several MeV energy solar origin  $Fe^{+12}$  at an  $L = 7$  outer boundary diffusing into Earth’s radiation belts by Spjeldvik et al. (2002) show that under equilibrium conditions, lower sw $Fe$  charge states, e.g., sw $Fe^{+1:+4}$ , predominate in the radiation belt at 100–1000 keV and higher sw $Fe$  charge states, e.g., sw $Fe^{+8:+12}$ , are most prevalent at several tens of MeV and higher. CIR and solar flare ions arrive from and constitute additional components of solar origin which are not as continuous as the solar wind but easily supply a range of very energetic ions to Earth’s magnetosphere. Therefore, for simplicity, we initially consider

them as a sporadic high-energy tail of the solar wind ions, because any  $Fe^+$  contribution from them requires an amount of charge loss in Earth’s magnetosphere. Alternatively, radiation belt particles contain 1–4 MeV/amu  $Fe$ , assumed singly charged (Mazur et al., 2000), and these ions may scatter inelastically after interacting with Earth’s thermosphere/exosphere, thus contributing to our measurements after highly non-elastic collisions. However, we are not aware that radiation belt particles can lose sufficient energy in collisions to become suprathermal energy ions. Spjeldvik (1979, 1996) discussed the entry, charge exchange, and presence of heavy ions in the inner magnetosphere. Beyond these studies, to our knowledge, prior to these works and ours, no other studies have endeavored to consider the charge exchange interactions of sw $Fe$  in and/or interior to the ring current-plasmasphere region of the near-Earth magnetosphere. Magnetospheric neutral particle populations might also contribute to our measured  $Fe^+$ , but outflow of these particles is not well characterized yet. Unlike thermal energy atomic and molecular populations whose intensity maximum can often help identify nearby charged and neutral particle sources, suprathermal ion intensities are often shaped by magnetospheric dynamics and ion acceleration is sometimes far from the origin. For example, ionospheric ions, once escaped from their low-altitude origins, can be accelerated at locations in the magnetotail by extant processes, such as current sheet acceleration, further increasing their energies and redistributing them globally. Consequently, suprathermal energy ions from various sources are often thoroughly mixed when measured.

Geotail measures  $Fe^+$ , as well as energized ionospheric  $N^+$ ,  $O^+$ , and  $MI^+$  from  $\sim 9 R_E$ , usually well inside the magnetopause, to its apogee at  $\sim 15 R_E$  sunward of the bow shock (see Figure 1 for the  $Fe^+$  observation locations). We investigate several characteristics of  $Fe^+$  in the near-Earth space, considering the relevance of the three possible sources noted above. Of the various research aspects resulting from this new look at long-term Geotail/STICS data,  $Fe^+$  is studied first because it is the minor ion most easily separated from other ion species in the measurements. Below, we discuss instrument characteristics and ion composition measurements in the  $\sim 9\text{--}30 R_E$  range relevant to the measurement of  $Fe^+$ . We then use these observations to demonstrate that (1) a portion of our observed  $Fe^+$  at Earth clearly does not obviously derive from HCS sw $Fe$  and that (2) the primary known inner source ion species,  $C^+$ , is typically not observed by either Geotail/STICS or Cassini/CHEMS in interplanetary space. Therefore, given no other likely sources, an important portion of

the observed  $\text{Fe}^+$  probably derives primarily from the abundant ablated cosmic material that collects at low altitudes in Earth's ionosphere.

## 2. Spacecraft, Instruments, PHA Data, and Plasma Regime Identification

### 2.1. Spacecraft and Instruments

The suprathermal ion composition spectrometer sensor, STICS, of the energetic particles and ion composition instrument. EPIC (particle experiment), on board the Geotail spacecraft, measures positive atomic and molecular ions (Williams et al., 1994). STICS uses energy per charge filtering followed by measurements of time of flight and, at higher energies, kinetic energy deposited in solid state detectors. In this study we primarily use higher-energy data from  $\sim 36$  to  $237$  keV/e, in which iron ion charge states' mass per charge ( $M/Q$ ) and mass ( $M$ ) are determined, using various thresholds for different purposes. Total kinetic energy, energy-per-charge, and time-of-flight measurements of individual ions are combined with various telescope parameters to generate pulse height analysis events (PHAs). On board, PHA events are used to calculate  $M$  and  $M/Q$  indices of each measured ion for counting rate classification and determination. A subset of all onboard PHAs are transmitted every 3 s with their associated counting rates. This study uses only these transmitted PHA measurements to broadly characterize the composition of suprathermal ion populations in and near Earth's magnetosphere, as long-term fluxes for the necessary species have not yet been determined, collected, and verified. After investigating Earth's distant magnetotail plasmas and magnetic fields from 1992 to 1994 (see, e.g., Christon, Eastman, et al., 1998; Eastman et al., 1998; Nishida, 1994; Nishida & Mukai, 2015), Geotail was placed in an  $\sim 9$ – $30 R_E$ ,  $\sim 5.2$  day, near-equatorial orbit (see Figure 1) in early 1995, where STICS has been used to investigate near-Earth phenomena (see, e.g., Christon et al., 2000, 2002; Keika et al., 2004, 2005; Nosé et al., 2009; Ono et al., 2009), where it continues to operate to this day. Geotail's long-term orbit precession provides uniform spatial coverage of the near-Earth, near-equatorial plane.

We also use  $\sim 3$ – $167$  keV/e data from the charge-energy-mass spectrometer, CHEMS, on the Cassini spacecraft (Krimigis et al., 2004) primarily for comparison with respect to spatial aspects of the interplanetary detection of  $\text{Fe}^+$  and  $\text{swFe}$ . CHEMS and our CHEMS analysis procedures are described in Christon et al. (2013, 2015) and Christon, Hamilton, Mitchell, DiFabio, et al. (2014). Additional detailed information for STICS and CHEMS is in Tables S1–S3 and S5–S7, respectively, in the supporting information. Cassini/CHEMS, Geotail/STICS, and their functionally identical sibling Wind/STICS (used by Posner et al. (2002) to detect suprathermal  $\text{N}^+$  and  $\text{O}^+$  up to  $\sim 100 R_E$  sunward of Earth) are functionally identical physically and practically, except for small differences in energy,  $M$ , and  $M/Q$  ranges. CHEMS is functionally separated into three telescopes and STICS into six telescopes using uniquely crafted microchannel plates. Cassini's Earth flyby was too brief to allow a dedicated in situ intercalibration of these two instruments. Data in the  $3$ – $167$  keV/e range from Cassini's cruise to Saturn and in the  $\sim 4$ – $20 R_S$  portion of Saturn's magnetosphere is used herein. For reference, the planet Saturn, with a radius ratio to Earth of  $\sim 9.45$  (see [http://nssdc.gsfc.nasa.gov/planetary/factsheet/planet\\_table\\_ratio.html](http://nssdc.gsfc.nasa.gov/planetary/factsheet/planet_table_ratio.html)), would occupy much of the near-Earth magnetosphere, to within  $\sim 0.5 R_E$  of Earth's nominal  $\sim 10 R_E$  subsolar magnetopause standoff location.

### 2.2. PHA Data Set

Color  $M$  versus  $M/Q$  survey spectrograms of the PHA data from both instruments, such as those shown in Figure 2, are generated from raw PHA data files and used extensively in this study. These displays of the data allow the user to obtain both important general overall and specific detailed information about observed particle populations which is not readily elucidated from standard rate/flux line plot formats. (Larger versions of the Figure 2 plasma regime panels are in the supporting information.) Each analysis format has its strengths. The color bar in each spectrogram display is normalized to the data accumulation sample's peak-count pixel (which is colored black). When  $\text{H}^+$  is included, it is usually the dominant ion, followed by He ions and then  $\text{O}^+$  or  $\text{O}^{+6}$ . The Geotail/STICS data presented in Figure 2 have been visually reviewed at a daily sample cadence. Daily production spectrograms of both instruments' data are routinely generated for instrument health assessment. Data for days with significant noise and/or signal anomalies, such as intervals with intense solar flare or geomagnetic-induced backgrounds, were removed from this analysis data set. This culling left 7427 daily files from 1995-060 to 2015-365 for use in this analysis. For this study, we obtain relevant ion species PHA counts in rectangular  $M$  versus  $M/Q$  boxes over 3 h intervals time synced to  $Kp$  geomagnetic index intervals for the mission duration, collecting sums for all times when STICS data was telemetered, deleting major

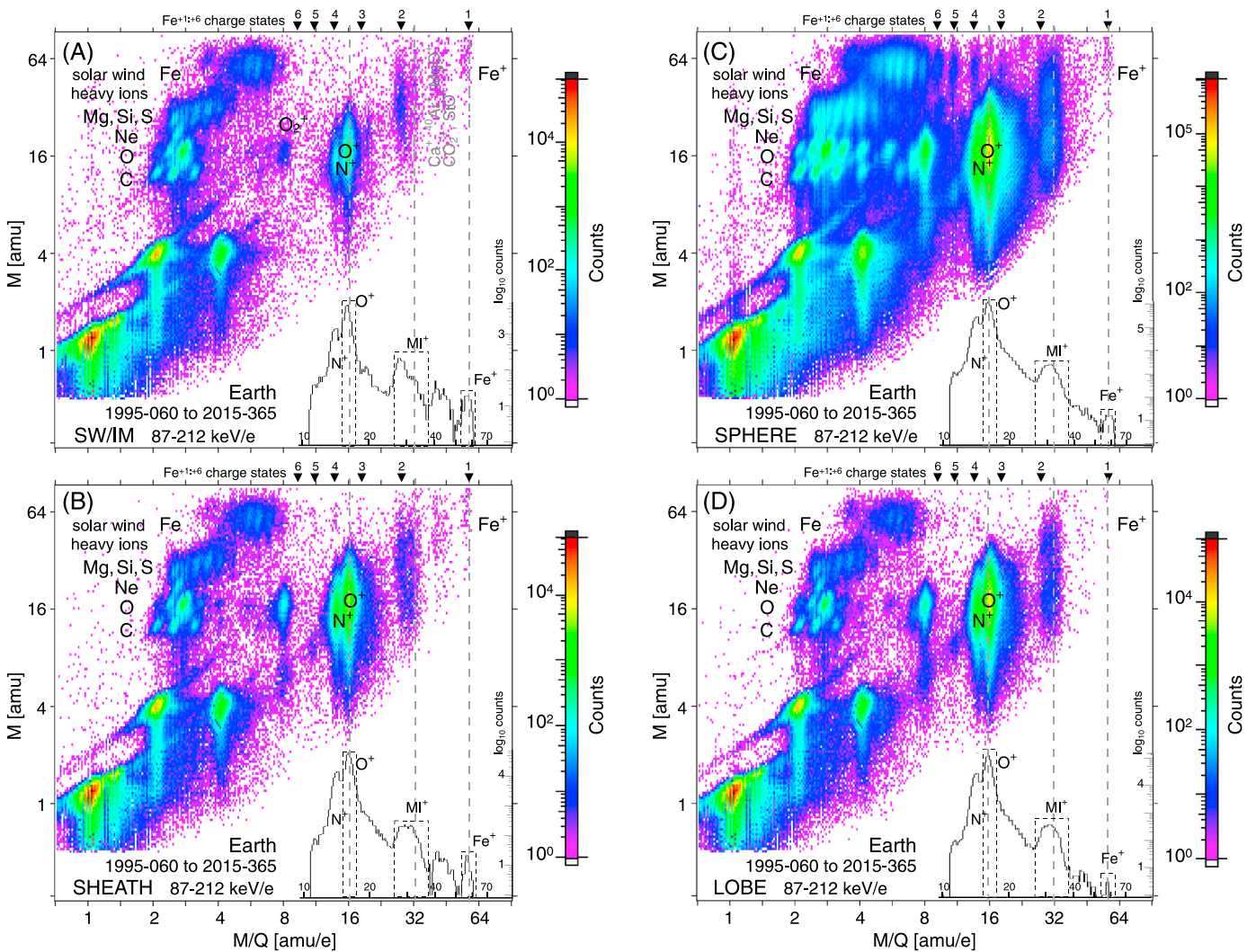


**Figure 2.** Suprathermal (87–212 keV/e) ion pulse height analysis, PHA, data obtained in and near Earth’s magnetosphere in two different plasma regime environment selections are displayed (see text for details). (a) SW/IM locations are outside the bow shock, the outer boundary of the principal Earth-solar wind/interplanetary medium interaction. (b) The SHEATH is inside the bow shock and outside the magnetopause. (c) The SPHERE includes regimes inside the magnetopause except for the lobe and magnetosphere boundary layers. (d) The LOBE is inside the magnetospheric boundary layer and outside the SPHERE’s higher-density plasmas. Triangles with numbers at top indicate expected  $M/Q$  locations of solar wind Fe charge exchange secondaries. Relevant heavy ion species are labeled. Histograms of the  $\geq 10$  amu/e data are shown; dashed boxes show the  $M/Q$  range for  $Fe^+/O^+$  and  $Fe^+/MI^+$  ratios given in the text. Only approximate relative abundances of ion species at  $M/Q \geq 10.85$  amu/e can be extracted directly from this display (see text). Larger versions of Figure 2 plasma regime panels are in the supporting information.

gaps. Practically, this results in a total STICS database of about 60,000 3 h sums, distributed from  $\sim 9$  to  $\sim 30 R_E$  around the Earth. Geotail naturally spends more time per orbit at apogee than perigee as a result of normal orbit dynamics, allowing additional observation time near  $\sim 30 R_E$  both in the upstream foreshock solar wind and in the deep magnetotail. In order to assess the overall characteristics of the data set in this initial study, we have ordered Geotail locations by plasma regime in the geocentric solar ecliptic, GSE, coordinate system (see supporting information). STICS rate and PHA data are ordered by and collected onboard in three overall basic rate (BR) channels, BR0, BR1, and BR2 (Williams et al., 1994), whose  $M$ - $M/Q$  basic ranges are shown in Figure S1 and listed Table S2 in the supporting information. Long-term basic rate and species rate PHA sums (for overall and major ions, respectively) are collected from the 1 day files. As a consequence of different instrumental energy thresholds, dissimilar particle energy distributions, telemetry constraints, and the onboard priority sampling scheme only approximate relative abundances of ion species in different basic rate ranges can be extracted directly from the displays in this paper. We show for reference, but do

not analyze, the BR2 light ions,  $H^+$ ,  $He^+$ , and  $He^{+2}$ , in several figures. The histograms in Figure 2 panels are normalized to the peak count bin.

Several background noise/interference signals are evident and most easily identified for the more abundant species, such as diagonal streaks from lower left to the upper right emanating from some species, the pillar of counts at all  $M$  values above  $H^+$  ( $M/Q \sim 1$  amu) in the magnetosphere (SPHERE, Figure 2c), and a signature, likely accidental coincidences, near  $M \sim 5$  amu,  $M/Q \sim 8$  amu/e in all plasma regimes' data except the solar wind (SW/IM, Figure 2a). Many of these background signals occur near perigee during geomagnetically active times and will be filtered out in later studies. Additionally, data collected during the  $22.5^\circ$  spacecraft spin sector when PHA and counting rate data for the previous spin is transmitted to the data processing unit is not used because of an engineering error. This sector is pointed  $\sim 25^\circ$  duskward of the Sun direction. Please note that the number of measured PHAs is shown in the figures and are not "livetime corrected," that is, the PHA counts are not corrected for livetime differences between the number of PHA counts and the various number of basic rate channel rate counts (which includes all measured ions), although since all  $N^+$  and  $O^+$  and  $\sim 50\%$  of the  $Fe^+$  are in BR1, the measured number of  $Fe^+$  is most likely a lower limit for the final number of livetime-corrected  $Fe^+$  counts used in statistical calculations for comparison to the HCS swFe ions, especially in the magnetosphere where  $O^+$  dominates all heavy ions. Please note, in particular, that the  $M/Q$  location of  $Fe^{+5}$  spans a heavy ion basic rate boundary in both STICS and CHEMS, 10.85 and 10.9 amu/e, respectively, so that the  $Fe^{+5}$   $M/Q$  distribution range is divided approximately in half by the HCS solar wind heavy—LCS ionospheric heavy basic rate boundary. All arguments relevant to the presence or absence of various ion species and/or their charge states can be and are made without the calculation of differential flux or number density, quantities which will be calculated and presented in future publications. Any arguments about the statistical significance of these ion species' observations depend on the observed ion species' particle counts presented in this paper not on the subsequently derived quantities such as differential flux or number density.

### 2.3. Near-Earth Plasma Regime Classification

Four broad plasma regime classifications are used to order STICS data with respect to location of observation in and near Earth's magnetosphere. They are the following: solar wind/interplanetary medium (SW/IM), magnetosheath (SHEATH), magnetosphere (SPHERE), and the somewhat emptier magnetospheric lobes (LOBE). We utilize the NASA Satellite Situation Center (SSC) Spacecraft Region Identification utility to classify and separate the data by their plasma regime identification scheme. The SSC utility identifies spacecraft regions visited by a spacecraft, using plasma and magnetic field data from the target spacecraft and other near-Earth spacecraft, as well as ground measurements ([http://sscweb.gsfc.nasa.gov/users\\_guide/ssc\\_reg\\_doc.html](http://sscweb.gsfc.nasa.gov/users_guide/ssc_reg_doc.html)). The SSC provides a dynamic data-based prediction representation of the average state and morphology of Earth's three-dimensional magnetospheric shape in the time-varying solar wind utilizing available spacecraft measurements (including those from Geotail) of the solar wind speed ( $V_{sw}$ ), density ( $N_{sw}$ ), and direction and magnitude of the interplanetary magnetic field ( $B_{IMF}$ ), in the OMNI data set (<http://omniweb.gsfc.nasa.gov>). For Geotail data, the SSC provides this spacecraft region identification in segments at a 12 min cadence. In Figure 2, we do not include 3 h intervals that contain any 12 min subintervals identified as magnetospheric boundary layers. We only use intervals when Geotail was most likely to be solely inside one of the four broad plasma regime classes noted above during each 12 min subinterval. In order to present certain arguments in subsequent analysis in this and later publications, we vary the energy, spatial, and/or species ranges used; however, Figure 2 presents the clearest, most general, yet focused data presentation with respect to location variations of the Fe data. In and around Earth's magnetosphere, these plasma regimes can have local observation intervals as short as several minutes in some locations, while at other times and/or locations, one plasma regime can be sampled continuously on the order of many hours to a day or so, depending on the plasma regime and the spacecraft location (for a detailed plasma regime analysis of the deep tail phase of the Geotail mission, see Eastman et al. (1998) and Christon, Eastman, et al., 1998). The overall plasma regimes chosen for this investigation are a superset of the SSC region identification classifications (see Figure 1 and Table S8 for details of the regime assignments in the supporting information). Our SW/IM, SHEATH, and LOBE regimes are the same as the SSC's regions of the same name. Our SPHERE regime contains the SSC's dayside magnetosphere, nightside magnetosphere, and plasma sheet regions. Figure S13 compares our regime assignments to Geotail key parameter data for two sample orbits. This model-based regime

identification is not perfect, but the most important aspect of our adopted procedure is that the SW/IM and SPHERE regimes are clearly separated, with boundary and overlapped/mixed region intervals possibly excluded, by utilizing the service developed by NASA and applied to all near-Earth spacecraft at the SSC.

Herein, we identify data as being in a specific regime where all SSC identifications within a 3 h interval are only locations classified as being in the same plasma regime. This excludes any intervals in which even one 12 min segment is not in the same regime as the other segments in the 3 h interval. We are left with a simple, straightforward, and clear classification method by imposing this restriction, focusing on observations obtained in distinct environments which may have readily identifiable and significant differences resulting from the plasma regime differences. This is especially important in the interplanetary (SW/IM) intervals in order to detect escaped magnetospheric origin ions. We found that looser plasma regime identification criterion restrictions did not ensure sufficient regime separation. We checked the magnetospheric contamination of the SW/IM data set to ensure that SW/IM data was not contaminated by proximity to the bow shock by collecting a restricted subset of SW/IM data at  $X_{GSE} > 20 R_E$ , a distance  $>5 R_E$  sunward of the nominal subsolar bow shock apex. Figure S4 in the supporting information compares observations selected at  $X_{GSE} > 20 R_E$  (purposefully  $\sim 5 R_E$  sunward of the nominal bow shock's local influence) to the overall randomly collected SW/IM data set. The strict SW/IM data overall contains approximately one third fewer PHA events and gives us the cleanest sample of unshocked solar wind obtainable with Geotail/STICS. This comparison reveals no large differences between the suprathermal solar wind ion composition closer or further from Earth sunward of the magnetopause, although escaped solar wind charge exchange secondaries are nearly indistinguishable from randomly occurring background in the  $X_{GSE} > 20 R_E$  data, if at all detectable. Other than that, there appears to be minimal difference between the solar wind samples. The spatial extent of charge exchange secondaries beyond the magnetopause will be determined in a future publication.  $Fe^{+1}$  is clearly visible in the  $X_{GSE} > 20 R_E$  foreshock solar wind data, as are  $O^+$ ,  $N^+$ , and  $MI^+$ . Below, we explore the characteristics of the  $Fe^+$  population and investigate its relationship, if any, to the three possible sources and differences, if any, between  $Fe^+$  in the various plasma regimes.

### 3. Observations

#### 3.1. Characterize Suprathermal $Fe^+$ Near Earth

Color spectrograms in Figure 2 show  $\sim 21$  years of 87–212 keV/e ion composition obtained from 1995–060, start of the  $9 \times 30 R_E$  near-Earth orbit, proceeding continuously to 2015–365. The plasma regime sorted data are presented in the following order: SW/IM, SHEATH, SPHERE, and LOBE. Ions from both the ionosphere and the solar wind are apparent in all four regimes.  $M/Q$  values of  $Fe^{+1:+6}$  in our instrument are identified by small triangles at the top axes in Figure 2. Heavy ion species relevant to this analysis are labeled in black, several other possible species are labeled in gray, and light ions are unlabeled. Histograms in the lower right-hand corner of the spectrograms show all PHA events at  $M/Q \geq 10.8$  amu/e, data which are in a single basic rate classification, BR1, and share the same livetime in each instrument collection cycle. These histogram data can therefore be separated, selected, and directly intercompared in order to estimate rough composition ratios, such as  $Fe^+/O^+$ . While all ion species and all four plasma regimes are shown, the main focus of this study is primarily on similarities of and differences between the SPHERE and SW/IM data relevant to observation of  $Fe^+$ , swFe, and swFe charge exchange secondaries. Below, we address the regimes, SPHERE, SW/IM, SHEATH, and LOBE, in order of importance to understanding the possible origin of  $Fe^+$ .  $Fe^+$  is distinctly evident and identifiable in each plasma regime.

While relatively weak, the  $Fe^+$  signal is distinct and statistically significant in all regions except the LOBE, where it is almost absent. The SPHERE data selection, Figure 2c, at Earth is analogous to our data selection for Saturn's magnetosphere (Christon et al., 2015), containing the magnetotail plasma sheet, quasi-trapping region (Christon, Hamilton, et al., 1994), main phase ring current (Andreeva & Tsyganenko, 2016; Daglis et al., 1999; Le et al., 2004), and other near-Earth locations. For ions with  $M \geq 10$  (mostly the upper half of the panels), relatively more charge exchange secondaries (e.g., for swFe these are  $Fe^{+3:+6}$ ) appear in the SPHERE than in any other regime because the interacting/sourcing neutral particle populations for the secondaries are strongest in the SPHERE. While  $Fe^{+3:+6}$  are clearly present in the SPHERE at  $\sim 87$ –212 keV/e, at slightly lower instrument energy channels,  $\sim 56$ –87 keV/e, where one needs to make comparisons, there are significant instrumental backgrounds which make critical intercomparisons impossible for  $Fe^{+4}$  and

$\text{Fe}^{+3}$ . Further, while  $\text{Fe}^{+2}$  may be present in the SPHERE, it is masked by, and not readily separable from, the  $\text{MI}^+$  signal. We have not yet developed an accurate procedure to uniquely separate any 28 amu/e  $\text{Fe}^{+2}$  and/or possible ionospheric origin  $\text{Si}^{+1}$  (Plane et al., 2016) from the more abundant  $\text{MI}^+$  fluxes that are more often present than either the  $\text{Fe}^+$  or  $\text{Fe}^{+5:+6}$  fluxes. Below, we work around this interference by selecting intervals with clearly identified  $\text{Fe}^{+1}$  during intervals of the least prevalent  $\text{MI}^+$  flux.  $\text{O}^+$  and  $\text{N}^+$  are the most abundant ionospheric heavy ions at Earth, followed by  $\text{MI}^+$ . Almost all O and C charge states, an admixture of solar wind and ionosphere sources, are observed in Earth's magnetosphere, except for  $\text{C}^+$ , which, if present, is masked by the  $\text{N}^+$  peak and an  $\sim 10.8\text{--}11.5$  amu/e noise/interference signal. Finally, for reference, there appears to be a generally decreasing background with increasing  $M/Q$  between the  $\text{MI}^+$  and the  $\text{Fe}^+$  (see Figure 2c), although the histogram shows a slight, statistically insignificant feature near  $\sim 45$  amu/e.

The SW/IM  $\text{Fe}^+$  signal in Figure 2a is distinct and statistically significant. Only trace amounts of swFe charge exchange secondaries are suggested in SW/IM data compared to SPHERE data and may be just separable from random background (Figure S4 in the supporting information shows that sw $\text{Fe}^{+3:+6}$  are very weak, if present at all, in the strict solar wind sunward of the bow shock). For example, the  $\text{Fe}^{+3:+6}$  signals are clearly much weaker than the  $\text{Fe}^+$  signal, a situation very different from that in the SPHERE. In contrast, dominant ionospheric origin ions accelerated in the magnetosphere, such as  $\text{N}^+$ ,  $\text{O}^+$ , and  $\text{MI}^+$ , are evident throughout Geotail's orbital range. Solar wind O and C charge state secondaries, clearly present in the SPHERE, are only marginally present in the SHEATH and barely discernible in the SW/IM, showing that there is only weak leakage of the magnetospheric ions into the solar wind sunward of the bow shock, expanding, improving, and adding context to earlier findings (Christon et al., 2002; Posner et al., 2002). Interestingly, in the SW/IM, a distinct signal of several ion species is present in the  $\sim 40\text{--}48$  amu/e range, possibly  $^{40}\text{Ar}^+$  and  $\text{CO}_2^+$  from the ionosphere and/or  $\text{SiO}^+$ ,  $\text{K}^+$ , and/or  $\text{Ca}^+$  from Earth's singly ionized IDP populations (Gerding et al., 2001; Plane et al., 2016). The ions observed at our energies may result from energization in the magnetotail, at the polar cusps, or near the bow shock, or a combination thereof.

The  $\text{Fe}^+$  signal is weakest in the LOBE and strongest in the SW/IM. These two extremes are possibly related to the time spent in each regime, so we must consider the  $\text{Fe}^+$  sum to that of other species in each regime for a more meaningful comparison. The swFe primaries are present in all regimes, but the swFe secondaries clearly present in the SPHERE and somewhat less evident in the LOBE and probably the SHEATH, but in the SW/IM, swFe secondaries are close to, if not consistent with, the general SWIM background level. Solar wind O and C secondaries are present, but at low levels close to background, outside the SPHERE. Taking a rough ratio of sums over the  $\text{Fe}^+$ ,  $\text{O}^+$ , and  $\text{MI}^+$  peaks in the four plasma regime histograms (see dashed boxes in Figure 2 histograms) results in the following, ratios with respect to  $\text{O}^+$  (see Table S9b):  $\text{Fe}^+/\text{O}_{\text{SW/IM}}^+ \approx 4.3 \times 10^{-3}$  ( $\pm 9\%$ ),  $\text{Fe}^+/\text{O}_{\text{SHEATH}}^+ \approx 2.4 \times 10^{-4}$  ( $\pm 13\%$ ),  $\text{Fe}^+/\text{O}_{\text{SPHERE}}^+ \approx 1.8 \times 10^{-5}$  ( $\pm 10\%$ ), and  $\text{Fe}^+/\text{O}_{\text{LOBE}}^+ \approx 1.3 \times 10^{-5}$  ( $\pm 38\%$ ); and  $\text{MI}^+$ :  $\text{Fe}^+/\text{MI}_{\text{SW/IM}}^+ \approx 7.5 \times 10^{-2}$  ( $\pm 9\%$ ),  $\text{Fe}^+/\text{MI}_{\text{SHEATH}}^+ \approx 2.5 \times 10^{-2}$  ( $\pm 13\%$ ),  $\text{Fe}^+/\text{MI}_{\text{SPHERE}}^+ \approx 3.8 \times 10^{-3}$  ( $\pm 10\%$ ), and  $\text{Fe}^+/\text{MI}_{\text{LOBE}}^+ \approx 1.8 \times 10^{-3}$  ( $\pm 38\%$ ). Ratios of  $\text{Fe}^+$  with respect to  $\text{MI}^+$  are consistent with ratios to  $\text{O}^+$ ; however, while still dominant, relatively fewer  $\text{O}^+$  are measured in the SW/IM in our energy range than in the SPHERE, so that both  $\text{Fe}^+$  and  $\text{MI}^+$  ratios to  $\text{O}^+$  are higher in the SW/IM than in the other regimes. The uncertainties above reflect the counting statistics of the  $\text{Fe}^+$  alone (values are from Table S9 in the supporting information). Although these rough ratios are neither rigorous nor precise evaluations, they show that with respect to these three species, as one might expect: SPHERE and LOBE data are very similar, and SHEATH data, intermediate between SW/IM and SPHERE, are closer to SW/IM data than SPHERE data. The similarity of the SW/IM and SHEATH ratios may indicate that at these energies, relatively fewer SPHERE than SW/IM ions are represented in the SHEATH data overall, or simply, that more  $\text{O}^+$  in the SW/IM is at lower energies invisible to STICS.

The relationship of yearly averaged  $\text{N}^+/\text{O}^+$  and  $\text{Fe}^+$  to the solar and geomagnetic indices  $F_{10.7}$  and  $Kp$  is shown in Figures 3a and 3b, respectively. (Please note that  $10 \times Kp$  is used.)  $\text{N}^+/\text{O}^+$ , recording the relationship of the two primary outflowing ionospheric heavy ions, is lower near solar maxima and higher near solar minima as a result of relatively stronger  $\text{O}^+$  than  $\text{N}^+$  outflow during solar maxima as shown in Figure 3c (see also Christon et al., 2002; Mall et al., 2002). Figures 3c and 3d show the time histories over two solar cycles of  $\text{N}^+/\text{O}^+$ ,  $\text{Fe}^+$ , and the solar and geomagnetic indices  $F_{10.7}$  and  $Kp$ , respectively. (Please note that for reference, Figure S2 in the supporting information shows several other solar and geomagnetic indices plotted versus time from

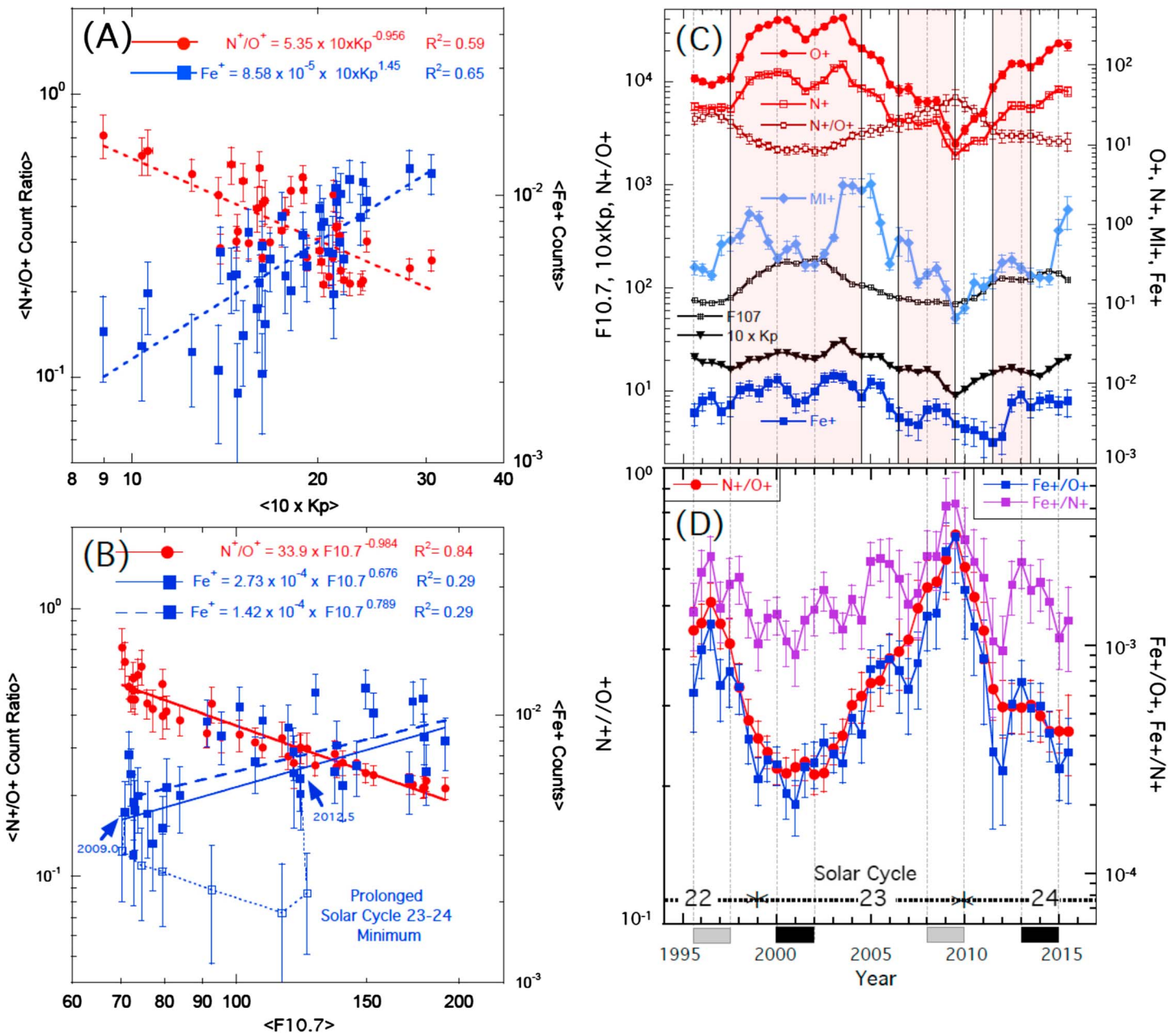


**Figure 3.** (a and b) Scatterplots of 1 year moving averages, stepped every half year, of Geotail/STICS  $N^+/O^+$  and  $Fe^+$  data versus average  $10 \times Kp$  (Figure 3a) and  $F_{10.7}$  (Figure 3b). Uncertainties shown are standard error of the mean. In Figure 3a  $10 \times Kp$  is plotted, where for example, near  $Kp = 2$  values are  $10 \times Kp$  ( $2-, 2o,$  and  $2+$ ) = 17, 20, and 23, respectively). In Figure 3b, open symbols identify  $Fe^+$  data from the prolonged solar cycle 23–24 minimum.  $F_{10.7}$ - $Fe^+$  solar minimum data start and end times shown are the midpoints times of the points arrows indicate. Power law fits are discussed in the text. (c and d) Plotted versus time are 1 year moving averages of Geotail/STICS suprathermal ions and solar and geomagnetic indices Figure 3c,  $F_{10.7}$  and  $10 \times Kp$ , respectively, and ion ratios (Figure 3d).  $N^+/O^+$ , plotted in both panels, exhibits a well-documented solar cycle variation. Ion data are from inside and outside the magnetosphere. Intervals of long-term contemporary  $Fe^+$  and other ions' roughly correlated variations are highlighted by shaded boxes in Figure 3c. Dark and light shaded boxes at the bottom and dashed lines, respectively, show approximate maximum and minimum solar activity intervals. Uncertainties shown are the moving averages' standard error of the mean.

1991 to 2016.) We use 1 year moving averages of 3 h sums stepped every half year in all panels of Figure 3 to characterize the  $Fe^+$  time variation which is sporadic on short and long time scales (Figure 3c) but, while sparse, generally continuous throughout each calendar year.  $Fe^+$  is somewhat more linearly correlated with  $Kp$  than with  $F_{10.7}$ , and although both distributions are widely scattered, they are positively associated with  $Kp$  in a statistical sense. It is apparent that the  $N^+/O^+$  is strongly, linearly correlated with  $F_{10.7}$ , but only

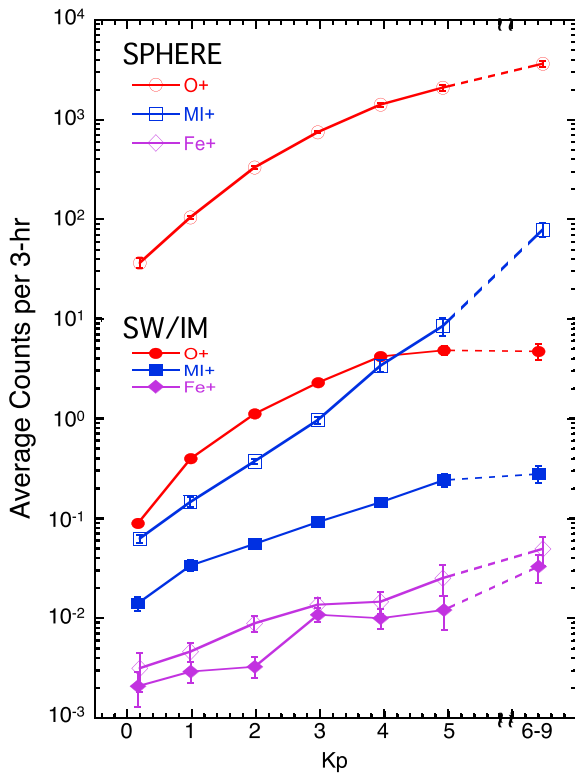


**Figure 4.** Average count rates (proportional to flux) of suprathermal ions in the SPHERE and SW/IM plasma regimes are plotted versus the average  $Kp$  (see text). Uncertainties shown are standard error of the mean. All species show an increase with  $Kp$  in both regimes. The rates in the sphere are higher than in the solar wind. Short dash color lines connect to the highest point which has a wider average  $Kp$  range, including  $6 \leq Kp \leq 9$ .

weakly corrected with  $Kp$ , both in a negative sense. On the other hand,  $Fe^+$  is positively associated with  $F_{10.7}$ , but its dependence is weak. It appears that there may be two  $Fe^+$  response clusters with respect to  $F_{10.7}$ , a low-count, low- $F_{10.7}$  group, and a higher-count, higher- $F_{10.7}$  group. Figure 2d suggests that  $\langle Kp \rangle$ , yearly averages, appears to shift to a lower overall level of activity, in concert with  $\langle F_{10.7} \rangle$  after the prolonged solar cycle 23–24 minimum. Power law fits to  $Fe^+$  counts in Figure 3b, one including all intervals and one excluding 2009.0 to 2012.5, much of the solar cycle minimum and the following recovery, show that exclusion of the solar cycle minimum data does not improve the linear correlation coefficient. This suggests that the  $Fe^+$  distribution is dominated by the broad scattering of the entire  $Fe^+$  response to  $F_{10.7}$  throughout. A cursory examination of the ion time histories shows that the lowest, most dramatic departure of  $Fe^+$  from a power law relationship/correlation with average  $F_{10.7}$  occurs during the prolonged solar cycle 23–24 activity minimum and recovery interval (shown by empty  $Fe^+$  counts symbols in Figure 3b). During Solar Cycle 23 maximum, 2000–2001,  $Fe^+$  experiences a significant decrease which is contemporaneous with a small, apparently anomalous,  $N^+/O^+$  increase. These different, but possibly linked  $Fe^+$  and  $N^+/O^+$  features will be investigated when the full data set is reprocessed for flux calculations and different, more adaptive, species separation methods can be applied. Despite relatively poor  $Fe^+$  count statistics and the large  $Fe^+$  amplitude variation during solar cycle 23 maximum, comparison of broad  $Fe^+$  rate averages over the two solar maxima and two solar minima identified in Figure 3, result in a near-significant sample  $T$  statistic of 2.34, where the critical values of the Welch  $T$  statistic, 1.96, 2.58, and 3.29, separate ranges in which the difference between two means is insignificant, just significant, significant, or highly significant, respectively, and the population variances are unknown (Mack, 1975). Alternately, addressing the apparent clustering of the  $Fe^+$  data, averages over the two apparent low- $F_{10.7}$  and

high- $F_{10.7}$   $Fe^+$  clusters in Figure 3b are significantly different statistically (see Figure S12 in the supporting information), irrespective of whether or how one combines the three most egregious outliers from 2009 to 2012.5 noted in Figure 3b. Thus, evidence currently extracted from these data suggests that the average number of  $Fe^+$  counts is positively associated with both average  $Kp$  and  $F_{10.7}$ , but the dependence on  $F_{10.7}$  is weaker overall, although one cannot rule out some amount of cross correlation between  $F_{10.7}$  and  $Kp$  (see Figure S3c in the supporting information).

The overall solar cycle dependence of  $Fe^+$  is consistent with both the  $Fe^+$  being more likely to escape a heated ionosphere at solar maximum and/or enhanced supplies of HCS swFe and/or ISPU1 brought to the magnetosphere by higher speed solar origin flows from near solar maximum through the declining phase of the solar cycle, where the increased  $Kp$  during the declining phase of  $F_{10.7}$  is the well-known effect of high-speed solar wind streams and their associated CIRs on the magnetosphere.) Investigating geomagnetic correlation further, we plot in Figure 4 averages of the  $O^+$ ,  $MI^+$ , and  $Fe^+$  3 h rates for the SW/IM and SPHERE data as a function of average  $Kp$  (averaged over  $Kp^- \leq Kp \leq Kp^+$  for  $0 \leq Kp \leq 5$  and over  $6^- \leq Kp \leq 9$  for the highest point, where  $Kp^{+-}$  is the integer  $Kp$  value  $\pm 0.3$ ). All three ion rates increase with increasing  $Kp$  in both regions. The  $O^+$  and  $MI^+$  increases in the SPHERE are much greater than the  $Fe^+$  increase, but it is clear that the  $Fe^+$  rates in the SPHERE are ~40–50% higher than those in the SW/IM. Despite this, almost as many  $Fe^+$  PHAs are counted in the SW/IM as those counted in the SPHERE, 124 and 130 PHAs, respectively. This happens because Geotail spends ~53% more time in the SW/IM than in the SPHERE, mostly at apogee (see Figure 1).

### 3.2. Suprathermal Ionospheric Origin $Fe^+$

We now seek to answer the question: Can one find intervals when ioFe, and neither swFe nor puFe, is the obvious  $Fe^+$  source? If there are such intervals, do they represent a significant portion of the data set?

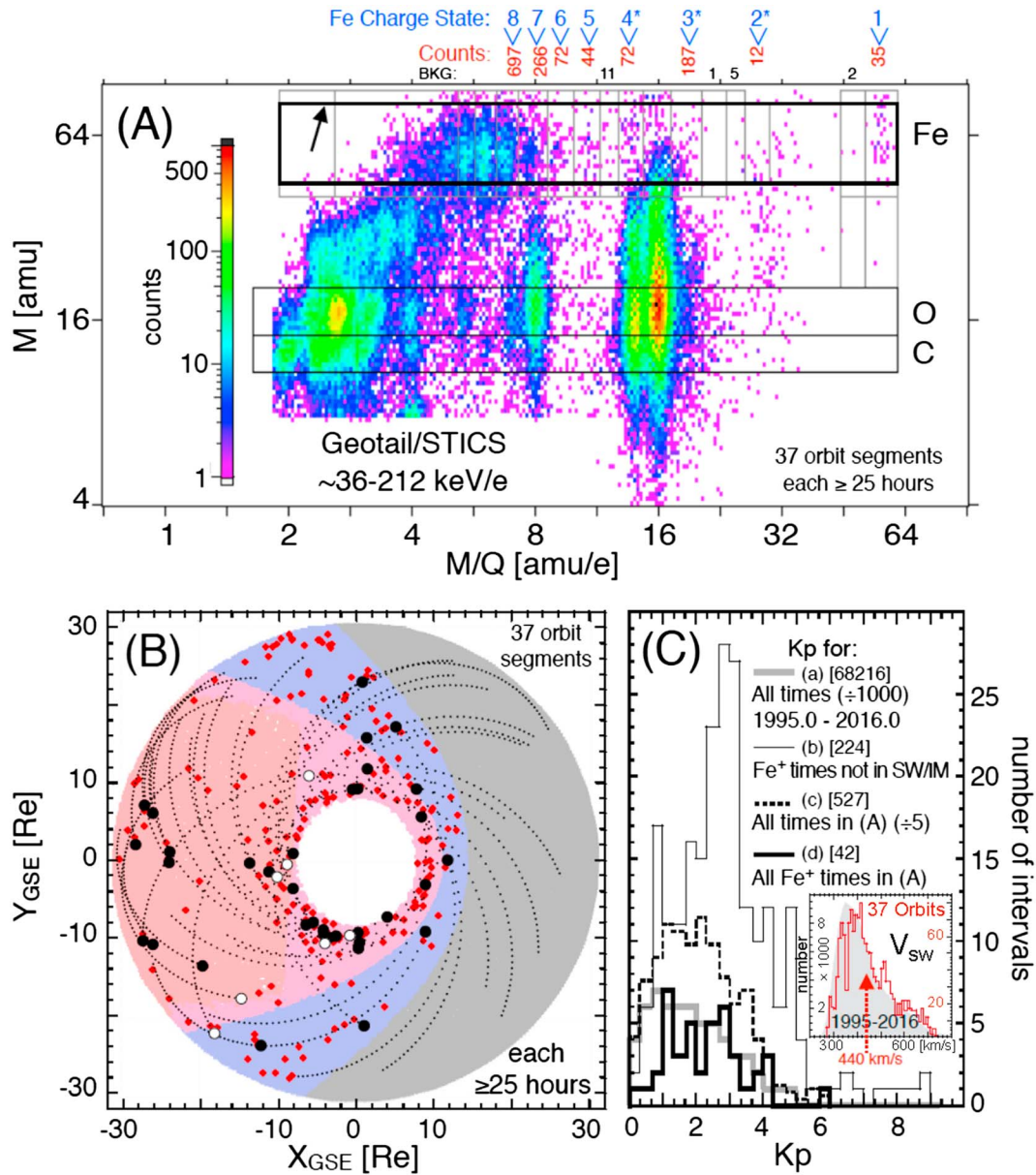


**Figure 5.** (a) At times of lower molecular ion flow, 37 orbit segments longer than 25 h (~70% of which are ≥36 h) were selected to capture any prior solar wind flows with swFe and/or ISPU Fe<sup>+</sup> that could result in the Fe<sup>+</sup> observed in the SPHERE and/or the SHEATH—the most likely regimes to observe Fe<sup>+2:+6</sup>. The main criterion used to choose these intervals was a minimal molecular ion presence in the Fe<sup>+2</sup> box. Fe<sup>+1:+8</sup> and background counts from collection boxes inside the heavy black boundary (shown by arrow) and vertical gray boundaries separating Fe charge states and background boxes are given above (Figure 5a). (b) Hourly points (small black dots) identify the orbit segments. Large dots identify measured Fe<sup>+</sup> locations, where black (open) dots indicate Fe<sup>+</sup> PHAs (not) in the principal Fe<sup>+</sup> collection box in (Figure 5a). Small red dots identify the other Fe<sup>+</sup> locations in these two regimes. (c) Histograms compare Kp for times of: (a) all data 1995-060 to 2016-001, (b) all measured Fe<sup>+</sup> not in SW/IM, (c) all data in (Figure 5a), and (d) only Fe<sup>+</sup> data in (Figure 5a); inset shows solar wind speed V<sub>sw</sub> for all data and for times of the 37 orbit segments.

swFe, puFe, and ioFe fluxes all should increase with the appearance of solar wind streams at Earth's orbit and, as we have shown above that an increase in average number of Fe<sup>+</sup> is correlated with Kp. It is instructive to ask whether a sufficient amount of Fe<sup>+</sup> is detected when the magnetosphere is not highly disturbed by solar wind stream disturbances. If HCS swFe is the source of the observed Fe, there should be a clear procession of secondaries from the HCS swFe ions down to Fe<sup>+</sup>, the Q<sub>Fe</sub> = 1 component. For example, this progression of charge states is almost fully demonstrated for core swC. In the SWIM (Figure 2a) swC has charge states 6 ≥ Q<sub>C</sub> ≥ 4, and swC<sup>+4:+6</sup> gains two to four electrons to produce the C<sup>+2</sup> observed in the SPHERE (Figure 2c) and analyzed previously (see Figure S3 and discussion in Christon, Hamilton, et al. (1994). In the present

examination of this data set, we cannot reliably determine  $C^{+1}$  during higher flux intervals as a result of STICS instrumental noise. Core swO consists of  $O^{+6:+8}$  and loses charge down to  $O^{+3}$  (Christon, Hamilton, et al., 1994; Gloeckler & Hamilton, 1987), but because  $O^{+2}$  and  $ioO^{+1}$  are strong in the SPHERE, charge exchanged sw $O^{+2}$  is inseparable from terrestrial origin  $O^{+2}$  in this examination of the data.  $O^{+2}$  may result from charge exchange of  $O^{+}$  or from energization of plasmaspheric  $O^{+2}$  (Geiss & Young, 1981). On the other hand, the solar wind Mg-Si-S group, dominated by swSi (Ko et al., 2014), does appear to gain four, possibly five, electrons in SPHERE data before its detection is masked by  $ioN^{+}$ ,  $ioO^{+}$ , and  $ioMI^{+}$ . Therefore, it is possible that sw $Fe^{+6}$  could also gain four, possibly five, electrons in order to become sw $Fe^{+2}$  or sw $Fe^{+1}$ .

In order to investigate whether there are times when  $Fe^{+}$  most likely results from an ionospheric source or from a solar wind introduced source, we adopt a search methodology based on the expectation that, given a known population of  $Fe^{+1}$  presumably derived from HCS sw $Fe$ , the  $Fe^{+1}$  should have recently derived from a comparable or greater population of sw $Fe^{+2}$ , and so on back up to sw $Fe^{+7:+14}$ . Therefore, it is necessary to identify sw $Fe$  charge state secondary populations that would necessarily lead to any sw $Fe^{+1}$ . In order to do this, we (1) extend the energy acceptance range to  $\sim 56$ – $210$  keV/e and (2) select 37 orbit segments shown in Figure 5b for a subset of  $Fe^{+}$  ions observed in the SPHERE or SHEATH at times of lower  $N^{+}$ ,  $O^{+}$ , and  $MI^{+}$  fluxes, which are also times of lower geomagnetic disturbance levels on the average (see Figure 4). Figure 5a is a color spectrogram of all heavy ion PHAs measured in the 56–212 keV/e  $E/Q$  range on the 37 orbit segments (Figure 5b). Figure 5c shows that the  $Kp$  and solar wind speed,  $V_{sw}$ , dependences of the selected orbits appear typical of the overall moderate to average  $Kp$  and nominal  $V_{sw}$  distributions of the full data set and do not represent a sample of atypically low  $Kp$  values. The  $Kp$  range  $0 \leq Kp \leq 4$  includes a dominant portion of all  $Fe^{+}$  times in Figure 5a, the selected orbit segments, and of all  $Fe^{+}$  times not in the SW/IM from 1995 to 2015, histograms 4Cd and 4Cb, respectively. In Figure 5a a heavy bordered box is drawn to identify a conservative collection region in which the mass range contains most  $Fe$  ions that we will call “prime”  $Fe$  ions. Gray vertical lines are drawn to separate  $Fe$  charge states and a few regions of random background. The number of prime PHA counts for relevant  $Fe$  charge states is given in red above Figure 5a, and counts in several background boxes are given in black below the charge state numbers. The deflection voltage (DV) energy step range threshold was decreased to  $\sim 56$  keV/e in order to detect as many sw $Fe^{+2:+5}$  ions as possible which might charge exchange into  $Fe^{+}$  ions in STICS’s nominal energy step configuration (see, e.g., Table S4). The energy range of data in Figure 5 includes, for example, DV18(56 keV/e)  $\sim 223$  keV  $Fe^{+4}$  ions which charge exchange into near-DV30(214 keV/e)  $\sim 223$  keV  $Fe^{+1}$  ions, close to STICS deflection voltage, DV, energy steps; or DV14(36 keV/e) 214 keV  $Fe^{+6}$  ions which charge exchange into near-DV30(212 keV/e) 214 keV  $Fe^{+1}$  ions; or alternately, DV14(36 keV/e) 178 keV  $Fe^{+5}$  ions which charge exchange into near-DV22(87 keV/e) 178 keV  $Fe^{+2}$  ions; all reasonably close to one of the nominal deflection voltage step energies. (We assume here that an ion’s total energy remains constant on the average during a charge loss interaction but may increase adiabatically between charge exchange interactions.) Then, as a result of instrument detection characteristics discussed above in section 2, portions of the  $Fe^{+4}$ ,  $Fe^{+3}$ , and  $Fe^{+2}$  signal locations are masked in the higher mass ranges of the  $N^{+}$ ,  $O^{+}$ , and  $MI^{+}$  PHA distributions (see also Figure 2c), respectively. The most important selection criterion is that the data for Figure 5 must include times of lower  $MI^{+}$  flux, which presents a weaker background than either  $N^{+}$  or  $O^{+}$  and, therefore, is easier to work around. Those readers wishing to bypass further details of our selection process and continue with the data analysis should proceed to the next paragraph. We include from 24 to 47 h prior to, and the hour of,  $Fe^{+}$  observation. That is, the selected orbit segments (Figure 5b) consist of the full day prior to the day of the  $Fe^{+}$  observation and the day of the  $Fe^{+}$  observation up to and including the hour of the  $Fe^{+}$  observation, resulting in 25–48 h orbit segments. In several cases two  $Fe^{+}$  are observed in less than 24 h, so that a longer interval containing both  $Fe^{+}$  observations and the 24 h before the first  $Fe^{+}$  observation is used. We note that any core solar wind and/or solar wind transported pickup ions entering Earth’s magnetosphere during any level of geomagnetic activity are likely to be energized to suprathermal energies ( $\sim 100$  keV/e) as are eV energy ionospheric ions, either at the cusp (Chen & Fritz, 2001; Fritz et al., 2003) or in Earth’s magnetotail (Christon, Hamilton, et al., 1994, Christon, Gloeckler, et al., 1994, Christon, Cohen, et al., 1998) by current sheet acceleration and adiabatic acceleration by earthward radial transport while conserving the first and second adiabatic invariants (Christon, Hamilton, et al., 1994). Charge loss processes from sw $Fe^{+ \geq 7}$  down to sw $Fe^{+6:+1}$  ( $+6 \geq Q_{Fe} \geq +1$ ) will occur in the

near-Earth magnetosphere where the exospheric hydrogen density,  $N_H$ , is spatially asymmetric and temporally variable out to at least  $\sim 8 R_E$ , as recently determined by Zoennchen et al. (2015) (see, e.g., Figure S5 in the supporting information) and Bailey and Gruntman (2011, 2013). Charge loss can occur at variable rates and is not readily evaluated, given (1) a spatially variable  $\leq 5\text{--}20\%$  nightside  $N_H$  peak at  $R < \sim 6.75 R_E$  and (2) the exosphere's overall order of  $\sim 2 (\pm 15\%)$   $N_H$  variations over a solar cycle (see Zoennchen et al., 2015, Figures 11 and 14) and (3)  $\sim 0.3\text{--}1.3$  day-long  $N_H$  increases of  $\sim 6\text{--}16\%$  at  $\sim 3\text{--}8 R_E$  during intense geomagnetic storms (Bailey & Gruntman, 2013).

Figure 5b orbit segments contain a total of 42  $\text{Fe}^+$  PHAs, which are about a quarter ( $\sim 26\%$ ) of the 162  $\text{Fe}^+$  measured inside the SPHERE and SHEATH (see Table S9). This number of selected  $\text{Fe}^+$  intervals having reduced  $\text{MI}^+$  flux as a necessary condition to assess the presence of  $\text{Fe}^{+2}$  is sufficient to make several firm statistical arguments. Note that the number of prime Fe PHAs in the  $\text{Fe}^{+4}$  and  $\text{Fe}^{+3}$  boxes, 72 and 187, respectively (red numbers at the top of Figure 5a), is clearly greater than the number of prime  $\text{Fe}^{+5}$  PHAs, 44, and likely contain significant background contributions from  $\text{N}^+$  and  $\text{O}^+$ , respectively, even at these low disturbance levels, and most likely do not represent a disjointed charge exchange process, that is, dissimilar to the regular, decreasing intensity progressions observed for swC, swO, and swSi in Figure 2c. This demonstrates that even with our careful selection procedure, we cannot currently use the prime  $\text{Fe}^{+4}$  and  $\text{Fe}^{+3}$  PHAs in this analysis.

We initially treat all prime PHAs in the  $\text{Fe}^+$  and  $\text{Fe}^{+2}$  boxes as  $\text{Fe}^+$  and  $\text{Fe}^{+2}$ , respectively, ignoring both the random background and the fact that many of the prime  $\text{Fe}^{+2}$  box counts are probably  $\text{MI}^+$  PHAs. One finds 35  $\text{Fe}^+$  and 12  $\text{Fe}^{+2}$  prime PHA counts. Defining a  $T$  statistic for the difference between two PHA count samples as  $T(\text{Fe}^+, \text{Fe}^{+2}) \equiv T(35, 12) = ((35 - 12) / \sqrt{(35 + 12)}) = (23 / 6.85) = 3.35$ , one finds that the number of  $\text{Fe}^+$  is larger than the number of  $\text{Fe}^{+2}$  in a statistically significant sense. Remember, that in STICS, the  $\text{Fe}^{+2}$  atomic ion has approximately the same measured  $M/Q$  as the  $\text{NO}^+$  molecular ion. Second, if one simply assumes that counts in the background boxes adjacent to the prime  $\text{Fe}^+$  and  $\text{Fe}^{+2}$  boxes at lower  $M/Q$  values represent the random background in the respective prime Fe boxes, the  $\text{Fe}^+$  and  $\text{Fe}^{+2}$  box counts become 33 and 7, respectively, and the difference between the two,  $T(33, 7) = 4.11$ , is very significant statistically. Finally, considering that many of the remaining PHAs in the prime  $\text{Fe}^{+2}$  box are likely  $\text{MI}^+$  ( $\text{N}_2^+$ ) ions by noting that a comparable number of  $\text{MI}^+$  ( $\text{NO}^+$ ) ions, 14, are present at higher  $M/Q$  in an equal-relative-width ( $\text{NO}^+$ ) box adjacent to the prime  $\text{Fe}^{+2}$  box, very few, if any, actual  $\text{Fe}^{+2}$  ions are possibly present in the  $\text{Fe}^{+2}$  box.

A complementary argument indicating that  $\text{Fe}^+$  is not of solar wind origin is to consider  $\text{Fe}^{+5}$ , a charge exchange secondary that does not have the  $\text{Fe}^{+2+4}$  background problems, and its possible relation to  $\text{Fe}^+$ . The  $T$  statistic comparing the difference between the 35  $\text{Fe}^+$  and 44  $\text{Fe}^{+5}$  prime PHAs is  $T(44, 35) = 1.01$ , indicating that their count difference is statistically insignificant. It is unlikely that the prime  $\text{Fe}^+$  population represented by its 35 count sample is charge exchanged from the prime  $\text{Fe}^{+5}$  population represented by its 44 count sample. We are not aware of any comprehensive observational or theoretical determinations of swFe charge exchange secondary ratios in Earth's  $\sim 7\text{--}10 R_E$  magnetosphere. Therefore, while remembering that  $\text{Fe}^{+6}$  is very rare in the solar wind (see Figure 2a), as a third complementary argument one may roughly estimate the number of  $\text{Fe}^+$  from the sw $\text{Fe}^{+6+7}$  data by considering charge exchange estimates based solely on the observed ratio of sw $\text{Fe}^{+6}$  to sw $\text{Fe}^{+7}$ . Note also that the following comparison represents a lower limit for  $\text{Fe}^+$  because the livetime correction for the  $\sim 50\%$  of sw $\text{Fe}^{+5}$  PHAs from BR1 in Figure 5 intervals would be greater than the livetime correction for the  $\sim 50\%$  of sw $\text{Fe}^{+5}$  BRO PHAs (refer to instrument discussion in section 2.2). Using the ratio of prime swFe ions,  $\text{Fe}^{+6}/\text{Fe}^{+7}$  ( $72/286 \sim 0.25$ ), as representative of losses at each charge exchange step, from  $Q = +6$  down to  $Q = +1$ , one would find  $\leq 1$  prime sw $\text{Fe}^+$ . Alternatively, using the ratio of prime  $\text{Fe}^{+5}/\text{Fe}^{+6}$  ( $44/72 \sim 0.61$ ) as representative, one would find  $\sim 6$  prime sw $\text{Fe}^+$  ions. These two estimates are much lower than both the 35 observed prime  $\text{Fe}^+$  and the 12 possible prime  $\text{Fe}^{+2}$  measured. These estimates, based merely on our measurements, would allow the possibility of several sw $\text{Fe}^+$  in the observations. Nevertheless, based on the first two, more solidly statistical arguments, we conclude that these  $\text{Fe}^+$  ions are highly unlikely to derive from the HCS swFe at these times, given the lack of any indication of an orderly progression of charge state secondaries downward from the HCS sw $\text{Fe}^{+7+14}$  source. The third argument above is also consistent with this conclusion.

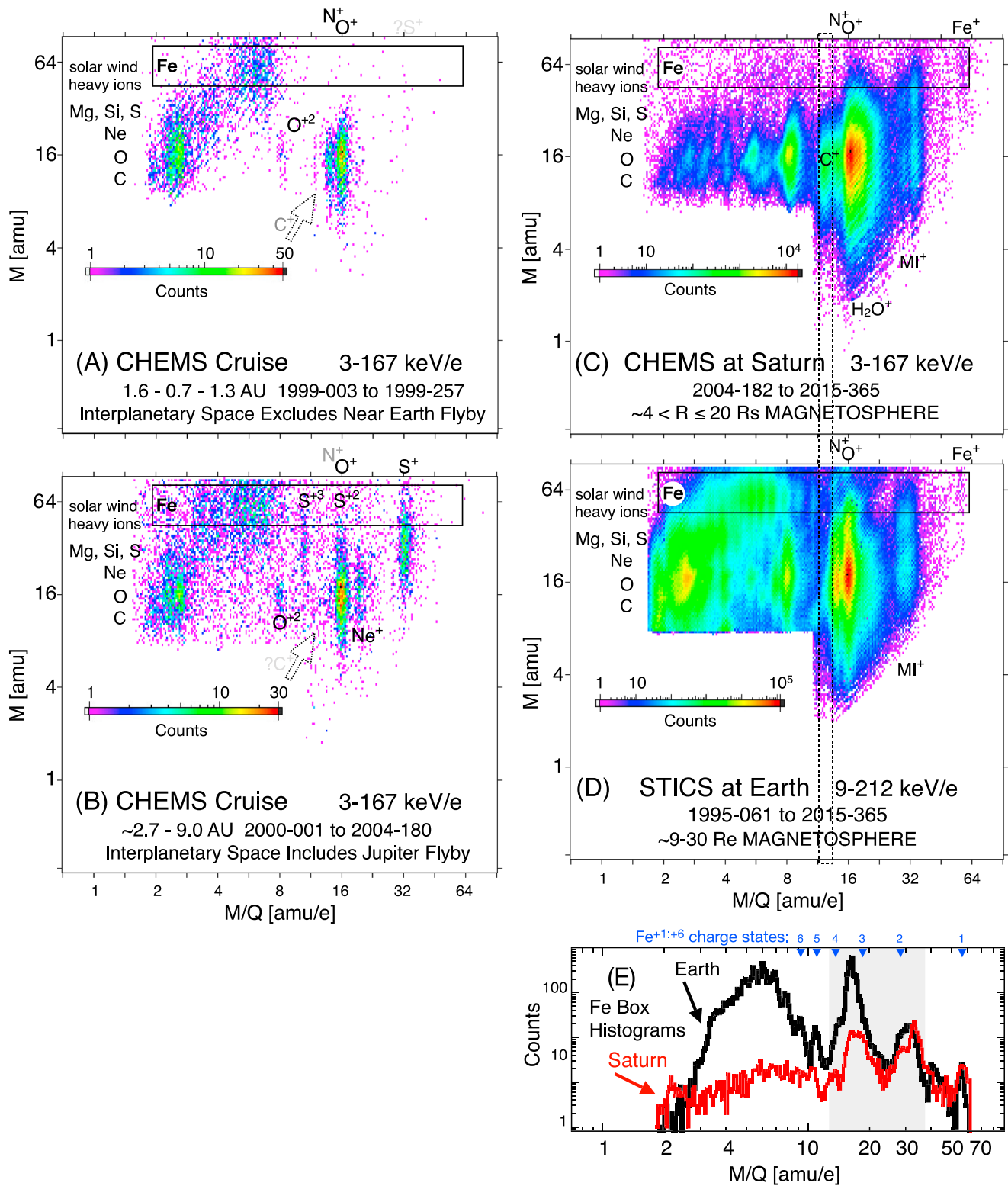


**Figure 6.** Long-term measurements of suprathermal energy heavy ions measured on Cassini’s cruise to Saturn through interplanetary space in (a) in 1999, 41 days in the inner heliosphere, including the flyby of Earth, and (b) from 2000 to mid-2004, ~4.5 years in the outer heliosphere, including the flyby of Jupiter in 2001, compared to data in the magnetospheres of (c) Saturn by Cassini, and (d) Earth by Geotail. Fe<sup>+</sup> is present at Earth and Saturn but not in interplanetary space. Dashed arrows in Figures 6a and 6b show the expected location of pickup C<sup>+</sup> at M/Q ~ 12 amu/e. Cassini’s passes by Earth and Jupiter were too brief to detect any extant Fe<sup>+</sup>. High-charge-state solar wind Fe is often present in Earth’s magnetosphere, but little solar wind Fe was detected in Saturn’s magnetosphere. (e) Histograms compare Fe box data from Saturn (Figure 6b) and Earth (Figure 6c). The M/Q range of likely N<sup>+</sup>, O<sup>+</sup>, and MI<sup>+</sup> spillover backgrounds masking Fe data is shaded.

### 3.3. Suprathermal Inner Source Ions Observed Near Earth

The above analysis shows that during the moderate geomagnetic activity levels having lower  $MI^+$  masking and moderate to low  $V_{sw}$  and  $Kp$  conditions that were examined,  $ioFe^+$  is more likely observed at Earth than  $swFe^+$ .  $swFe^+$  is probably absent in those time intervals. Inner source  $puFe^+$ , if it exists, would be most likely inseparable from  $ioFe^+$ , just as  $puO^+$  and  $swO^+$  are inseparable in the spectrogram. Now in order to demonstrate whether STICS detects any inner source ions when it detects the  $42 Fe^+$ , we examine the select 37 orbit segment Figure 5 data for  $puC^+$ , one of the two principal, most abundant inner source ions, which we use as a possibly more easily detected proxy for  $puFe^+$ . Given its several tens of keV threshold for detecting  $C^+$  in triple coincidence PHAs, it is unlikely that STICS can make this determination, and consequently, as might be expected, Figure 5a shows no detected  $C^+$  in our 37-orbit PHA sample of SW/IM, SHEATH, and SPHERE samples. Figure 5c inset shows that average  $V_{sw}$  of the 37 orbit segments is  $\sim 440$  km/s, and the STICS response to  $puC^+$  and  $puFe^+$  is, as expected, negligible. At lower solar wind speeds, ISPUI ions are not energetic enough for STICS to detect them (see supporting information Figures S8 and S9a). However, ISPUI species possibly energized at Earth's bow shock (e.g., Oka et al., 2002), in near-Earth turbulence and/or in Earth's magnetosphere when and if they enter with core solar wind ions (see e.g., Fujimoto et al., 1998; Terasawa et al., 1997), should be further accelerated in Earth's magnetosphere. Regardless, STICS does not detect ISPUI  $C^+$  during the select orbit segments. Background instrumental interference during higher geomagnetic activity intervals makes  $C^+$  analysis with STICS difficult.

In order to work around this, we enlist Cassini/CHEMS, an instrument functionally identical to STICS, but with a factor of  $\sim 3$  lower deflection energy threshold, to better detect  $puC^+$  at suprathermal energies (see Figures S8 and S9b). Figure 6a shows Cassini CHEMS interplanetary inner heliosphere data at  $\sim 0.7$ – $1.3$  AU in 1999, excluding the 3 h within  $\sim 15 R_E$  of Earth during its flyby ( $\sim 0330$  UT, 1999–230, see Figure S10a in the supporting information), an interval in which it is difficult to remove spurious background signals from the CHEMS data. Note that all measurement energies are used in Figure 6 for both instruments. CHEMS measured Earth associated fluxes on the day of Earth flyby and for a day or so afterward. Little data were obtained before Earth flyby; CHEMS became fully operational the day before Earth flyby. The solar wind speed,  $V_{sw}$ , increased from  $\sim 500$  km/s just before closest approach to  $\sim 700$  km/s about a day after Earth flyby, averaging  $\sim 610.5$  km/s (see Figure S10b in the supporting information). The dashed arrow in Figure 6a points to likely  $puC^+$  measured by CHEMS during Earth flyby. Note that  $puN^+$  and  $puO^+$  from the high-energy tail of the inner source would be indistinguishable from Earth's  $ioN^+$  and  $ioO^+$ . Of the  $\sim 26$  likely  $C^+$  PHAs measured, 20 were measured on day 1999–230 after the flyby during the high-speed stream and 6 were measured later, beyond Earth orbit. High  $V_{sw}$  in that stream increased the possibility that CHEMS would detect  $puC^+$ , and, apparently, it did. While  $puFe^+$  should be more readily detected by CHEMS than  $puC^+$ , that is, a heavier ion traveling at the same speed (see supporting information Figures S8 and S9), CHEMS detected no  $Fe^+$  during 1999. On the other hand, Geotail/STICS measured 2  $Fe^+$  and no  $C^+$  during the full 1999 Cassini Earth flyby interval, days 229 to 257, although, it is a simple matter to find numerous 28 day intervals when Geotail/STICS measures no  $Fe^+$ . CHEMS's small  $puC^+$  sample allows us to roughly estimate the ratio  $puFe^+/puC^+ \leq \sim 0.04 \pm 0.04$ , but it is much higher and less relevant than the long-term informal upper limit,  $Fe^+/C^+ \sim 0.005 \pm 0.005$  taken from data in Gloeckler et al. (2010) (see supporting information Table S10). With  $V_{sw} \geq \sim 610$  km/s after Earth flyby, CHEMS should have readily detected all inner source ion species fairly close to their density peaks, with the heavier ions detected more easily. While  $puC^+$  may be accelerated in Earth's magnetosphere, it was not readily measured by AMPTE/CCE/CHEM over an  $\sim 4$  month interval (see e.g., Figure S3 and Christon, Gloeckler, et al. (1994)) and does not appear to attain energies high enough for STICS to reliably detect it in the magnetosphere at moderate to low geomagnetic activity levels (Figure 5a).

Figures 6c and 6d compare long-term magnetospheric measurements at Saturn from Cassini ( $\sim 11.5$  years at  $\sim 4$ – $20 R_S$ ) and Earth from Geotail ( $\sim 21$  years at  $\sim 9$ – $30 R_E$ ), respectively. At Saturn, the low observation latitude constraints of CHEMS' earlier studies are relaxed (Christon et al., 2013, 2015; Christon, Hamilton, et al., 2014) and include all magnetospheric data within  $20 R_S$ . At Earth, we include SPHERE, LOBE, and mixtures of the two for a generally comparable sampling of regimes at the two planets. The dashed box drawn at the  $M/Q$  range of  $C^+$  over both panels highlights the fact that while a low-energy signature of Saturn's locally produced  $C^+$  is present, no comparably extended  $C^+$  signature (similar also to the weak  $puC^+$  signal in Figure 6a) can presently be discerned at Earth as a result of strong  $ioN^+$  spillover and extant instrumental background

masking part of the  $C^+$  region. Therefore, with no discernible inner source  $C^+$  signal measured at Earth over an  $\sim 21$  year interval using the entire STICS energy range, we find it unlikely that any measurable inner source  $Fe^+$  was detected either.

### 3.4. Is Suprathermal $Fe^+$ Observed Far From Earth and Saturn?

In order to demonstrate that suprathermal  $Fe^+$  appears to be uniquely associated with and local to the Earth and Saturn magnetospheres, complementary interplanetary space, and long-term measurements at those planets are now considered. This examination focuses primary attention on detection in interplanetary space of  $Fe^+$  and of ISPU ions which have been observed out to the orbit of Jupiter (Gloeckler & Geiss, 1998). Figures 6a and 6b show long-term heavy ion PHA sums of Cassini/CHEMS cruise data (a) during 1999,  $\sim 35$  days mostly after Earth flyby, excluding the  $\leq 14 R_E$  bow shock through magnetosphere portion of the flyby, and (b) all times from 2000-001,  $\sim 2$  AU, far away from any Earth  $Fe^+$  influence, through and including the Jupiter flyby, until day 2004-180 at  $\sim 9$  AU, about 2 days before Saturn encounter. Major solar flare intervals were excluded. As one can see in Figure 6b, CHEMS measures no trace of  $Fe^+$  far from Earth over the  $\sim 6.5$  years of cruise data. Figure 6c demonstrates clearly where the  $Fe^+$  distribution is located and the several PHAs measured in and near the  $Fe^+$  region in Figure 6b are consistent with nearby background levels. In contrast, the Ulysses spacecraft discovered inner source  $puC^+$  and  $puO^+$  on its way to its Jupiter flyby at  $\sim 5$  AU. The CHEMS data from  $\sim 2.7$  to  $\sim 9$  AU in Figure 6b reveal neither  $C^+$  nor  $Fe^+$  above background, an interval of  $\sim 4.5$  years. CHEMS detected Jovian  $S^+$  signatures from  $\sim 3$  months before until  $\sim 11$  months after Jupiter flyby, but CHEMS did not detect Saturn-origin ions until, possibly, the day before the first Saturn encounter. We presume this resulted from the highly structured  $B_{IMF}$  average direction at  $\sim 9$  AU, approximately normal to the heliocentric radial near the ecliptic plane, effectively directing most Saturn escaping particles away from Cassini's approach direction. However, CHEMS detected no  $Fe^+$  in interplanetary space.

It is notable that Cassini/CHEMS did not detect  $Fe^+$  at or near Jupiter (Figure 6b) where IDP metal layers are predicted (Kim et al., 2001) and  $Fe^+$  should therefore be present in Jupiter's ionosphere. Cassini's Jupiter flyby and near-planet magnetospheric interval were very brief, and this alone might explain the lack of  $Fe^+$  detection at Jupiter. Alternatively, it is likely more difficult for  $Fe^+$  to escape from Jupiter than from either Earth or Saturn because of Jupiter's greater gravitational pull,  $\sim 2.4$  times that at Saturn and/or Earth, where the gravitational pulls at one planetary radius are comparable to each other within  $\sim 8\text{--}9\%$  (see [https://nssdc.gsfc.nasa.gov/planetary/factsheet/planet\\_table\\_ratio.html](https://nssdc.gsfc.nasa.gov/planetary/factsheet/planet_table_ratio.html)). The principal heavy ions measured at Jupiter are  $O^+$  and  $S^+$ , ions which likely originate in Io's volcanic activity and not in Jupiter's atmosphere (Smyth & Marconi, 2003).

Considering Figures 6c and 6d,  $Fe^+$  measurements in the Saturn and Earth magnetospheres, respectively,  $Fe^+$  is distinctly present in both magnetospheres, although, at Saturn, the HCS swFe signal is not strong, being close to the random background noise (Figure 6e), while at Earth, HCS swFe primaries are clearly present. The low-level peak for  $Fe^{+5}$  in Figure 6e Saturn histogram suggests that swFe charge exchange secondaries, obviously present at Earth, may have a parallel, but less clearly detected, presence at Saturn.  $Fe^{+2:+4}$  data at Earth are masked by  $N^+$ ,  $O^+$ , and  $MI^+$  and by instrument backgrounds which may be removable or correctable. Compared to Earth, measured swFe at Saturn is weaker relative to measured  $O^+$  and barely present. The suprathermal HCS Mg-Si-S group, moderately strong at Earth, is also much weaker at Saturn. Noting the two very different solar wind environments at these planets, if swFe were a principal source of Earth's  $Fe^+$ , one might expect a stronger  $Fe^+$  signal at Earth.

Considering Figures 5a and 6d, we found the  $Fe^+$  and swFe secondary signal strengths in Figure 5a to be comparable at low to moderate geomagnetic activity; for example, the relative  $Fe^+$ -to- $Fe^{+5}$  signal in Figure 5a is 1 to  $\sim 1.25$  (i.e.,  $1 < Fe^+/Fe^{+5} < 1.25$ ). With the inclusion of the high geomagnetic activity intervals in Figure 6d, if swFe ions were a significant  $Fe^+$  source in the magnetosphere, one might anticipate a stronger  $Fe^+$ -to- $Fe^{+5}$  relative signal than the observed 1 to  $\sim 30$  ratio, i.e.,  $Fe^+/Fe^{+5} \sim 0.02$  (see Figure 6e).

Finally, as mentioned above, Gilbert et al. (2012) reported sw $Fe^{+2}$  in cold filament plasma embedded in CME solar wind events. Cold plasma is outside STICS' energy range. Nevertheless, we examined STICS suprathermal data on the days of and just after the Gilbert et al. (2012) intervals, in search of filament related higher-energy ion data. We observed the following: five intervals with no PHAs in the  $Fe^{+2}$  or  $Fe^{+1}$  boxes,

one interval with one  $\text{Fe}^{+1}$  but only molecular ions in the  $\text{Fe}^{+2}$  box, one interval with one  $\text{Fe}^{+2}$  but no  $\text{Fe}^{+1}$ , and a final interval with molecular ions in the  $\text{Fe}^{+2}$  box and no  $\text{Fe}^{+1}$  (see the Figure S6 color spectrograms in the supporting information). Therefore, we find no evidence of suprathermal  $\text{Fe}^{+1+2}$  associated with these cold filaments.

Summarizing the observations,  $\text{Fe}^{+}$  appears to originate at Earth and is distinctly present in three of the four plasma regimes near Earth with small, but readily identifiable, distributions at all geomagnetic levels. LOBE ion data have the smallest number of  $\text{Fe}^{+}$  PHAs. SW/IM data have the largest number of PHAs relative to  $\text{O}^{+}$  as a result of orbital dwell at apogees. Average  $\text{Fe}^{+}$  count rates in the SPHERE are greater than in the SW/IM, as are those of  $\text{O}^{+}$  and  $\text{MI}^{+}$ . The  $\text{swFe}^{+3:+6}$ , charge exchange secondaries that might help identify  $\text{swFe}$  as a possible source of  $\text{Fe}^{+}$ , are only abundant in the SPHERE but have small, nearly trace amounts in the other regimes, where their ratios relative to  $\text{Fe}^{+}$  are small.  $\text{Fe}^{+}$  is clearly present and  $\text{Fe}^{+2}$  is essentially absent during intervals selected for lower interference from major ionospheric species, about a quarter of all  $\text{Fe}^{+}$  observations inside the bow shock. During the same intervals,  $\text{swFe}^{+5}$  has numbers of PHA counts comparable to the number of  $\text{Fe}^{+1}$  PHA counts, consistent with the absence of  $\text{Fe}^{+2}$ , indicating that  $\text{Fe}^{+}$  does not derive from  $\text{swFe}$  at those times. In the SW/IM and SHEATH,  $\text{swFe}$  secondary signals are all closer to random background levels and less distinct than the respective  $\text{Fe}^{+}$  signal in that regime. In the LOBE, both  $\text{Fe}^{+}$  and  $\text{swFe}$  secondary signals are weak. Inner source  $\text{puC}^{+}$ , a primary inner source component, is likely present in the  $\sim 35$  days of data obtained after Cassini's Earth flyby during which no  $\text{Fe}^{+}$  was observed by Cassini/CHEMS which should have more readily detected  $\text{puFe}^{+}$  than  $\text{puC}^{+}$ . Our one-count upper limit estimate of inner source  $\text{puFe}^{+}/\text{puC}^{+}$  during that interval is an order of magnitude higher than a long-term upper limit estimate of  $\text{puFe}^{+}/\text{puC}^{+}$  from data reported by Gloeckler et al. (2010), consistent with a negligible inner source  $\text{Fe}^{+}$  component in Earth's magnetosphere. This leaves ionospheric origin  $\text{Fe}^{+}$  as the only practical explanation of the  $\text{Fe}^{+}$  in  $\sim 25\%$  of  $Kp < 4$   $\text{Fe}^{+}$  detections inside the magnetosphere.

#### 4. Discussion

$\text{Fe}^{+}$  is observed in all four major near-Earth plasma regimes. Solar wind origin  $\text{Fe}$  would be an obvious, natural source of  $\text{Fe}^{+}$  overall, if a clear, orderly progression of  $\text{swFe}$  charge exchange secondaries, from the high-charge-state nominal solar wind ions,  $\text{Fe}^{+27}$ , down through  $\text{Fe}^{+2}$ , were detectable during the times of decreased molecular ion flux masking at  $Kp < \sim 4$  that we examined. However, such an orderly  $\text{swFe}$  charge state progression was not observed for this  $\text{Fe}^{+}$  sample,  $\sim 26\%$  of all SPHERE and SHEATH  $\text{Fe}^{+}$  detections. No trace of the principle inner source ion  $\text{puC}^{+}$ , a proxy for  $\text{puFe}^{+}$ , was detected by Geotail during these selected  $\text{Fe}^{+}$  intervals either. Although the more sensitive Cassini charge mass ion spectrometer, CHEMS, likely detected inner source  $\text{puC}^{+}$  in one interval shortly after its Earth flyby in 1999, it did not measure any  $\text{puFe}^{+}$  in the same data. Neither did CHEMS measure any  $\text{Fe}^{+}$  in interplanetary space until it arrived at Saturn. Therefore, about approximately one fourth of all  $\text{Fe}^{+}$  observations inside Earth's bow shock do not support either a solar wind or inner source origin for the  $\text{Fe}^{+1}$ . That is, ionospheric origin  $\text{Fe}^{+}$  escaped from atmospheric layers accumulated from ablated IDP atom and ions is likely the origin of the suprathermal  $\text{Fe}^{+}$  observed during the selected low  $\text{MI}^{+}$  flux conditions. We have not determined whether solar wind  $\text{Fe}$  contributes to Earth's  $\text{Fe}^{+}$  during intervals of high geomagnetic activity as a result of high backgrounds.

Observations shown in Figure 3 strongly support an ionospheric origin interpretation of suprathermal  $\text{Fe}^{+}$ . The strong  $\text{Fe}^{+}$  and  $\text{O}^{+}$  decrease during the prolonged solar cycle 23–24 activity minimum and subsequent recovery appear to be temporally related. The solar cycle 23–24 minimum was much longer than expected and the thermosphere densities and temperatures were anomalously lower than during the several, most recent, previous solar cycles (Emmert et al., 2010, 2014). General similarities of the  $\text{O}^{+}$ ,  $\text{N}^{+}$ , and  $\text{Fe}^{+}$  time histories highlighted in Figure 3c suggest correlation, although correlation does not require a causal relationship. Several large-scale temporal variations are clearly in opposite directions, but overall, there are general similarities. The solar cycle 23–24  $\text{Fe}^{+}$  and  $\text{O}^{+}$  minima are out of sync, but their contemporaneous recovery profiles are somewhat similar from mid-2011 to mid-2013, after the  $F_{10.7}$  recovery is well on its way. Full investigation of the possible relationship between these ionospheric species during this interval is beyond the scope of this work, but the suprathermal ion data suggest that the behaviors and escape of a primary ionospheric component,  $\text{O}^{+}$ , and a minor ionospheric component,  $\text{Fe}^{+}$ , may be related through chemistry and the

physical/structural characteristics of the two populations. For example, the lifetime of  $\text{Fe}^+$  at metal layer altitudes is highly dependent on the concentration of atomic O via their chemical reactions (Plane et al., 2015). Although a detailed discussion of long-term solar control of thermospheric particles and chemistry is beyond the scope of this paper, the sum of a few known facts suggest that ionospheric  $\text{Fe}^+$  from the metal layers might be expected to exhibit a solar cycle variation. Plasma density (Liu et al., 2007) and upward ion flux in ion upflow events at  $>300$  km altitude (Ogawa et al., 2010) are highest during solar maximum. Although no solar cycle dependent  $\text{Fe}^+$  or Fe layer height variation is evident at  $\leq 110$ – $120$  km (see, e.g., Dawkins et al., 2016), any  $\text{Fe}^+$  at higher altitudes escaped from the metal layer should participate in extant particle dynamics. The known thermospheric density decrease at solar minima should result in fewer ionospheric particles escaping. Thermosphere/ionosphere density, temperature, and ion composition variations should naturally result in a solar cycle  $\text{Fe}^+$  upflow/outflow variation similar to that of principal ionospheric species that  $\text{Fe}^+$  chemistry involves, such as  $\text{O}^+$  and  $\text{N}^+$ . We have drawn a simple sketch summarizing several important aspects relevant to a possible solar cycle effect in ionosphere/thermosphere  $\text{Fe}^+$  concentration in Figure S11 in the supporting information; however, a fuller discussion of  $\text{Fe}^+$  upflow/outflow is deferred to a future, dedicated publication.

The present analysis has allowed us to define and address the  $\text{Fe}^+$  source question in a portion of the Geotail data, but it has not permitted us to unambiguously determine the balance of ionospheric and solar wind  $\text{Fe}^+$  sources during geomagnetically more active intervals when  $\text{Fe}^+$  was measured but the  $\text{Fe}^{+2:+4}$  signals are masked by the dominant ionospheric origin  $\text{N}^+$ ,  $\text{O}^+$ , and  $\text{MI}^+$ . Improved separation techniques may permit removal of the ionospheric distributions masking  $\text{Fe}^{+2:+4}$ , but that analysis would require subtraction of a large background (e.g.,  $\text{MI}^+$ ) from the observations to find a smaller signal (e.g.,  $\text{Fe}^{+2}$ ), and the resultant smaller signal's final uncertainty may likely be larger than the signal itself, rendering it at best an unreliable upper limit. Further, the traces of swFe charge exchange products in the SW/IM are weak compared to the strong  $\text{Fe}^+$  signal there and may be difficult to quantify. Modeling the escape probabilities and upstream transport of  $\text{Fe}^+$  and swFe secondaries should help to understand the data, but, to our knowledge, little experimental or theoretical work has been published on this topic.

Why the  $\text{puC}^+$  population is not detected in Earth's magnetosphere is another open question. Inner source ions are a minor signal in interplanetary space at solar wind energies, but Earth's magnetosphere, a fairly effective accelerator of low-energy ions, does not apparently accelerate  $\text{puC}^+$  to observable energies. This analysis shows that neither Geotail/STICS nor Cassini/CHEMS can demonstrate that inner source  $\text{Fe}^+$  is detected in the several tens to several hundred keV energy range during the intervals examined.

Although much general information results from the present analysis, various aspects of these data cannot readily be explained with the sum of existing observations, such as the abundance of ionospheric  $\text{MI}^+$  and  $\text{Fe}^+$  in our strict foreshock selection data. Several in situ studies have shown that ionospheric origin ions are a transient, yet persistent feature of the upstream region out to at least  $\sim 100$ – $200 R_E$  sunward of Earth and possibly beyond (e.g., Christon et al., 2000; Keika et al., 2004; Kronberg et al., 2011; Möbius et al., 1986; Posner et al., 2002). Recent studies from multispacecraft missions (e.g., Burch & Phan, 2016; Cassak & Fuselier, 2015; Dunlop et al., 2011; Fuselier et al., 2012; Trattner et al., 2016) show that magnetopause reconnection likely plays a large role in the ionospheric ion presence in the subsolar magnetosheath, with the furthest observations of magnetospheric particles related to heliocentric radial aligned interplanetary magnetic field directions (see Kronberg et al., 2011; Posner et al., 2002, and references therein). Interplanetary magnetic field and solar wind velocity components have typical spatial correlation lengths of  $\sim 0.5$ – $2 \times 10^6$  km ( $\sim 78$ – $313 R_E$ ) except for the radial component of  $V_{\text{sw}}$  and  $|B_{\text{IMF}}|$ , ranging from  $\sim 2$ – $7 \times 10^6$  km ( $\sim 313$  to  $\sim 1100 R_E$ ) (Wicks et al., 2010), so that sufficiently energetic particles can propagate upstream to the locations observed herein and further upstream at L1 in other studies. Geotail routinely detects  $\text{O}^+$ ,  $\text{N}^+$ ,  $\text{MI}^+$ , and  $\text{Fe}^+$  beyond the bow shock, ions originating primarily in Earth's ionosphere which have gyroradii slightly larger but generally comparable to those of the swFe secondaries. If the charge exchanged swFe secondaries observed equatorially in the SPHERE escape with and in the same manner as any equatorial  $\text{Fe}^+$ , such as through the dayside magnetopause where their gyroradii should be on the order of  $>0.5 R_E$  (see Table S7 and Figure S7), the swFe secondaries should also be observed in the SHEATH with strengths relative to  $\text{Fe}^+$  comparable to those observed in the SPHERE. Additionally,  $\text{Fe}^+/\text{MI}^+$  is comparable

to  $\text{M}^+/\text{O}^+$  in the each of the SPHERE, SHEATH, and SW/IM (Figure 2 and Table S9b), suggesting comparable overall escape scenarios and/or paths. Likewise, the same swFe secondary strengths relative to  $\text{Fe}^+$  should be expected at and upstream of the bow shock (see Figure 2 and Figure S4 in the supplementary information), but they are not. SPHERE swFe charge exchange secondaries do not appear to gain the same access to the SHEATH or SW/IM that the ionospheric species  $\text{O}^+$ ,  $\text{N}^+$ ,  $\text{M}^+$ , and  $\text{Fe}^+$  have otherwise more swFe charge exchange secondaries would be observed in the foreshock region. For reference, Figures 1 of Cohen et al. (2016) and Westlake et al. (2016), and their discussions, demonstrate that  $\text{O}^+$ , with a 1120 km gyroradius, appears to pass through an  $\sim 500$  km thick magnetopause, while  $\text{e}^-$ ,  $\text{H}^+$ , and  $\text{He}$ , with gyroradii smaller than the magnetopause thickness, appear to be locally contained or entrained in the magnetopause. In this specific case, 36 to 212 keV/e sw $\text{Fe}^{+2:+6}$  secondaries with gyroradii from 730 to 3083 km would be expected to pass through the magnetopause.

In addition to near-equatorial escape, it is likely that some  $\text{Fe}^+$  escapes Earth's high-latitude ionosphere in turbulence the auroral zone and/or near the cusp to be further accelerated in the magnetotail and/or gain access to upstream interplanetary magnetic field lines. Being a heavy ion,  $\text{Fe}^+$  would probably only access to the nearer-Earth magnetotail or the geosynchronous orbit region. This might explain some of the stronger  $\text{Fe}^+$  and relative weaker swFe secondary presence in the dayside magnetos heat and foreshock solar wind. Nilsson et al. (2004) have measured ionospheric  $\text{O}^+$  in the dayside cusp at energies up to  $\geq 38$  keV at altitudes of  $\sim 4\text{--}8 R_E$ . These ions have clearly been energized well above their low-altitude energies. The average outflowing  $\text{O}^+$  and  $\text{H}^+$  parallel velocities are nearly equal at  $\sim 75\text{--}200$  km/s for  $\sim 1$  h at  $\sim 7.6\text{--}8.7 R_E$ , with the  $\text{O}^+$  energy greater than and apparently coupled to the  $\text{H}^+$  energy, suggesting to us possible bulk outward plasma motion. Any  $\text{Fe}^+$  in these plasma flows would have probably had the same parallel velocity. The interested reader is referred to Nilsson et al. (2004) for their excellent introduction and analysis of these outflowing ions. This, coupled with the nominal several hundred Earth radii correlation length noted above, should provide adequate access to upstream regions to explain the observations highlighted in this study. Although suprathermal magnetospheric ions can readily escape through Earth's magnetopause into the magnetosheath (Cohen et al., 2016; Westlake et al., 2016), to our knowledge, the proportion of lower energy ionospheric ion or neutral outflow by various exit paths into the foreshock region relative to that transported into Earth's magnetosphere has not yet been quantified (Nilsson et al., 2012, 2013). It may be none or it may be sufficient to account for a portion of the observed upstream suprathermal ions. Various aspects of the above topics will be addressed after all species fluxes have been determined.

## 5. Concluding Remarks

We have discovered and investigated measurements of a rare ion,  $\text{Fe}^+$ , in and around Earth's magnetosphere. By classifying, separating, and analyzing the  $\text{Fe}^+$  observations with respect to magnetospheric plasma regimes and reducing several measurement backgrounds, we have shown that high-charge-state solar wind origin Fe is not a likely  $\text{Fe}^+$  source in about 25% of equatorial  $\text{Fe}^+$  observations inside the bow shock. Because possible inner source pickup  $\text{Fe}^+$  ions would likely be inseparable from ionospheric origin  $\text{Fe}^+$ , as a proxy for inner source  $\text{Fe}^+$  we alternatively searched for  $\text{C}^+$ , one of the two primary inner source ions, and find that  $\text{C}^+$  is not present in this selected data set. As a result, we conclude that neither solar wind Fe nor possible inner source  $\text{Fe}^+$  ions (anticipated but never measured) is a likely source of Earth's  $\text{Fe}^+$  during low to moderate geomagnetic activity. Comparison of the full magnetospheric data set at Earth to long-term data from Saturn's magnetosphere, where extant  $\text{Fe}^+$  and  $\text{C}^+$  magnetospheric origin populations have been measured by a functionally identical instrument for years, shows that no clear  $\text{C}^+$  population is obviously present at Earth. As a result, we tentatively rule out the inner source ions as a principal  $\text{Fe}^+$  source. We are not able to confirm solar wind Fe as a likely source of Earth's  $\text{Fe}^+$  during geomagnetically active intervals. Much of Earth's  $\text{Fe}^+$  probably escapes with extant ionospheric outflow from the ionospheric  $\text{Fe}^+$  layers that form at low altitudes produced by incoming interplanetary dust particles. This is similar to the process that apparently occurs at Saturn, a much larger magnetosphere. We conclude that ionospheric outflow of  $\text{Fe}^+$  from dust-ionosphere interaction processes probably occurs naturally at both planets and that outflow is the likely origin of suprathermal  $\text{Fe}^+$  in the magnetospheres of both planets.

## Glossary of Acronyms and Terms

BR*	basic rate $M$ versus $M/Q$ collection region (where * is 0–2 for STICS and 0–6 for CHEMS)
CHEMS	charge-energy-mass ion composition spectrometer on Cassini spacecraft
CIR	coronating interaction region between fast and slow solar wind streams
$E$	total ion kinetic energy
EPIC	particle experiment on the Geotail spacecraft in Earth orbit
$F_{10.7}$	solar activity index
IDP	interplanetary dust particle (dust, meteoroids, and comets)
io..., pu..., sw...,	prefixes distinguishing ionosphere, pickup, and solar wind source ions
ISPUI	inner source pickup ions from interplanetary dust
$K_p$	geomagnetic activity index
LOBE	part of magnetosphere where magnetic field pressure dominates
livetime correction	procedure to calculate ion charge state fluxes using PHAs and basic rates
$M$	ion mass determined from energy deposit and time of flight
$M/Q$	mass per charge determined from time of flight
magnetosphere	region where planetary magnetic field dominates
OSPUI	“outer source” pickup ions from interstellar sources
PHA	pulse height analyzed ion event measured by STICS or CHEMS
prime Fe PHA	a Fe PHA event in a restricted $M$ and $MPQ$ analysis range
$Q$	charge state of an ion
RID	(plasma) Regime IDentification (this acronym is only used in the supporting information)
SHEATH	turbulent region between magnetopause and bow shock
Solar Cycle	the ~11 year activity cycle of the Sun
SPHERE	part of magnetosphere where particle pressure dominates
STICS	charge-energy-mass ion composition spectrometer on Geotail spacecraft in Earth orbit
SW/IM	unshocked solar wind, interplanetary medium outside the bow shock
$V_{sw}$	solar wind velocity

### Acknowledgments

This work would not exist without the help of R. D. DiFabio, J. Gunther, S. E. Lasley, A. T. Y. Lui, C. E. Schlemm II, J. D. Vandegriff, and many others. We thank NASA for support through grant NNX13AE61G and NNN06AA01C(NA07). JMCP's work was supported by the European Research Council (project 291332—CODITA). The NASA plasma region identifications integrated into the locator form (<https://sscweb.gsfc.nasa.gov/cgi-bin/Locator.cgi>) for Geotail's orbital locations in and near Earth's magnetosphere were invaluable in this research. The Geotail/EPIC/STICS data set for 1992–2010 can be found at [http://pdf.gsfc.nasa.gov/pub/data/geotail/epic/stics\\_pha\\_ascii\\_gzip/](http://pdf.gsfc.nasa.gov/pub/data/geotail/epic/stics_pha_ascii_gzip/) and for later times at <http://sd-www.jhuapl.edu/Geotail/>. Geotail ephemeris data are at <http://sscweb.gsfc.nasa.gov/>. Solar and geomagnetic indices were obtained from both <http://omniweb.gsfc.nasa.gov/form/dx1.html> and <http://wdc.kugi.kyoto-u.ac.jp/dstae/>. The entire Cassini/MIMI/CHEMS data set and Cassini ephemeris data can be found at <http://pds.nasa.gov>.

### References

- Allegrini, F., Stewards, N. A., McComas, D. J., Gloeckler, G., & Geiss, J. (2005). Stability of the inner source pickup ions over the solar cycle. *Journal of Geophysical Research*, *110*, A05105. <https://doi.org/10.1029/2004JA010847>
- Andreeva, V. A., & Tsyganenko, N. A. (2016). Reconstructing the magnetosphere from data using radial basis functions. *Journal of Geophysical Research: Space Physics*, *121*, 2249–2263. <https://doi.org/10.1002/2015JA022242>
- Andrews, D. J., Edberg, N. J. T., Eriksson, A. I., Gurnett, D. A., Morgan, D., Nèmec, F., & Opgenoorth, H. J. (2015). Control of the topside Martian ionosphere by crustal magnetic fields. *Journal of Geophysical Research: Space Physics*, *120*, 3042–3058. <https://doi.org/10.1002/2014JA020703>
- Bailey, J., & Gruntman, M. (2011). Experimental study of exospheric hydrogen atom distributions by Lyman-alpha detectors on the TWINS mission. *Journal of Geophysical Research*, *116*, A09302. <https://doi.org/10.1029/2011JA016531>
- Bailey, J., & Gruntman, M. (2013). Observations of exosphere variations during geomagnetic storms. *Geophysical Research Letters*, *40*, 1907–1911. <https://doi.org/10.1002/grl.50443>
- Bame, S. J. (1972). Spacecraft observations of the solar wind composition. In C. P. Sonett, P. J. Coleman, & J. M. Wilcox (Eds.), *Solar Wind* (Vol. 427, pp. 535–558). Astrophysics and Space Science Library, NASA Special Publication, Washington, DC: Scientific and Technical Information Office. <http://adsabs.harvard.edu/abs/1972NASSP.308..535B>
- Benna, M., Mahaffy, P. R., Grebowsky, J. M., Plane, J. M. C., Yelle, R. V., & Jakosky, B. M. (2015). Metallic ions in the upper atmosphere of Mars from the passage of comet C/2013 A1 (Siding Spring). *Geophysical Research Letters*, *42*, 4670–4675. <https://doi.org/10.1002/2015GL064159>
- Berger, L., Drews, C., Taut, A., & Wimmer-Schweingruber, R. F. (2015). Short-term variability of inner-source pickup ions at 1 AU SOHO/CELIAS observations. *Astronomy and Astrophysics*, *576*, A54. <https://doi.org/10.1051/0004-6361/201425116>
- Burch, J. L., & Phan, T. D. (2016). Magnetic reconnection at the dayside magnetopause: Advances with MMS. *Geophysical Research Letters*, *43*, 8327–8338. <https://doi.org/10.1002/2016GL069787>
- Carrillo-Sánchez, J. D., Plane, J. M. C., Feng, W., Nesvorný, D., & Janches, D. (2015). On the size and velocity distribution of cosmic dust particles entering the atmosphere. *Geophysical Research Letters*, *42*, 6518–6525. <https://doi.org/10.1002/2015GL065149>
- Carter, L. N., & Forbes, J. M. (1999). Global transport and localized layering of metallic ions in the upper atmosphere. *Annals of Geophysics*, *17*, 190–209. <https://doi.org/10.1007/s00585-999-0190-6>
- Cassak, P., & Fuselier, S. A. (2015). Reconnection at Earth's dayside magnetopause. In W. Gonzalez, & E. Parker (Eds.), *Magnetic Reconnection* (Vol. 427 *Astrophys. Space Sci. Library*) (pp. 213–276). Berlin: Springer. [https://doi.org/10.1007/978-3-319-26432-5\\_6](https://doi.org/10.1007/978-3-319-26432-5_6)

- Chen, J., & Fritz, T. A. (2001). Energetic oxygen ions of ionospheric origin observed in the cusp. *Geophysical Research Letters*, *28*, 1459–1462. <https://doi.org/10.1029/2000GL012128>
- Christon, S. P., Gloeckler, G., Williams, D. J., Mukai, T., McEntire, R. W., Jacquey, C., ... Yamamoto, T. (1994). Energetic atomic and molecular ions of ionospheric origin observed in distant magnetotail flow-reversal events. *Geophysical Research Letters*, *21*, 3023–3026. <https://doi.org/10.1029/94GL02095>
- Christon, S. P., Hamilton, D. C., Gloeckler, G., Eastman, T. E., & Ipavich, F. M. (1994). High charge state carbon and oxygen ions in Earth's equatorial quasi-trapping region. *Journal of Geophysical Research*, *99*, 13,465–13,488. <https://doi.org/10.1029/93JA03328>
- Christon, S. P., Cohen, C. S., Gloeckler, G., Eastman, T. E., Galvin, A. B., Ipavich, F. M., ... Williams, D. J. (1998). Concurrent observations of high charge state solar wind oxygen ions in the magnetosphere and in interplanetary space during the 10–11 January 1997 magnetic cloud event: Geotail and Wind observations. *Geophysical Research Letters*, *25*, 2987–2990. <https://doi.org/10.1029/98GL01408>
- Christon, S. P., Eastman, T. E., Doke, T., Frank, L. A., Gloeckler, G., Kojima, H., ... Yamamoto, T. (1998). Magnetospheric plasma regimes identified using Geotail measurements. 2. Statistics, spatial distribution, and geomagnetic dependence. *Journal of Geophysical Research*, *103*, 23,521–23,542. <https://doi.org/10.1029/98JA01914>
- Christon, S. P., Desai, M. I., Eastman, T. E., Gloeckler, G., Kokubun, S., Lui, A. T. Y., ... Williams, D. J. (2000). Low-charge-state heavy ions upstream of Earth's bow shock and sunward flux of ionospheric  $O^{+1}$ ,  $N^{+1}$ , and  $O^{+2}$  ions: Geotail observations. *Geophysical Research Letters*, *27*, 2433–2436. <https://doi.org/10.1029/2000GL000039>
- Christon, S. P., Mall, U., Eastman, T. E., Gloeckler, G., Lui, A. T. Y., McEntire, R. W., & Roelof, E. C. (2002). Solar cycle and geomagnetic  $N^{+1}/O^{+1}$  variation in outer dayside magnetosphere: Possible relation to topside ionosphere. *Geophysical Research Letters*, *29*(5), 1058. <https://doi.org/10.1029/2001GL013988>
- Christon, S. P., Hamilton, D. C., DiFabio, R. D., Mitchell, D. G., Krimigis, S. M., & Jontof-Hutter, D. S. (2013). Saturn suprathermal  $O_2^+$  and mass- $28^+$  molecular ions: Long-term seasonal and solar variation. *Journal of Geophysical Research: Space Physics*, *118*, 3446–3463. <https://doi.org/10.1002/jgra.50383>
- Christon, S. P., Hamilton, D. C., Mitchell, D. G., DiFabio, R. D., & Krimigis, S. M. (2014). Suprathermal magnetospheric minor ions heavier than water at Saturn: Discovery of  $28M^+$  seasonal variations. *Journal of Geophysical Research: Space Physics*, *119*, 5662–5673. <https://doi.org/10.1002/2014JA020010>
- Christon, S. P., Hamilton, D. C., Mitchell, D. G., Plane, J. M. C., DiFabio, R. D., Krimigis, S. M., Nylund, S. R., & Lui, A. (2014). Discovery of suprathermal  $Fe^+$  in the magnetospheres of Earth and Saturn, paper presented at 2014 Fall Meeting, Abstract SM51D-4275, San Francisco, CA: American Geophysical Union, 15–19 Dec.
- Christon, S. P., Hamilton, D. C., Plane, J. M. C., Mitchell, D. G., DiFabio, R. D., & Krimigis, S. M. (2015). Discovery of suprathermal  $Fe^+$  in Saturn's magnetosphere. *Journal of Geophysical Research: Space Physics*, *120*, 2720–2738. <https://doi.org/10.1002/2014JA020906>
- Chu, X., Yu, Z., Gardner, C. S., Chen, C., & Fong, W. (2011). Lidar observations of neutral Fe layers and fast gravity waves in the thermosphere (110–155 km) at McMurdo (77.8°S, 166.7°E), Antarctica. *Geophysical Research Letters*, *38*, L23807. <https://doi.org/10.1029/2011GL050016>
- Cohen, I. J., Mauk, B. H., Anderson, B. J., Westlake, J. H., Sibeck, D. G., Giles, B. L., ... Burch, J. L. (2016). Observations of energetic particle escape at the magnetopause: Early results from the MMS Energetic Ion Spectrometer (EIS). *Geophysical Research Letters*, *43*, 5960–5968. <https://doi.org/10.1002/2016GL068689>
- Daglis, I. A., Thorne, R. M., Baumjohann, W., & Orsini, S. (1999). The terrestrial ring current: Origin, formation, and decay. *Reviews of Geophysics*, *37*, 407–438. <https://doi.org/10.1029/1999RG000009>
- Dawkins, E. C. M., Plane, J. M. C., Chipperfield, M. P., Feng, W., Marsh, D. R., Höffner, J., & Janches, D. (2016). Solar cycle response and long-term trends in the mesospheric metal layers. *Journal of Geophysical Research: Space Physics*, *121*, 7153–7165. <https://doi.org/10.1002/2016JA022522>
- Dhoms, S. S., Saunders, R. W., Tian, W., Chipperfield, M. P., & Plane, J. M. C. (2013). Plutonium-238 observations as a test of modeled transport and surface deposition of meteoric smoke particles. *Geophysical Research Letters*, *40*, 4454–4458. <https://doi.org/10.1002/grl.50840>
- Dunlop, M. W., Zhang, Q.-H., Bogdanova, Y. V., Trattner, K. J., Pu, Z., Hasegawa, H., ... Carr, C. (2011). Magnetopause reconnection across wide local time. *Annals of Geophysics*, *29*, 1683–1697. <https://doi.org/10.5194/angeo-29-1683-2011>
- Eastman, T. E., Christon, S. P., Doke, T., Frank, L. A., Gloeckler, G., Kojima, H., ... Yamamoto, T. (1998). Magnetospheric plasma regimes identified using Geotail measurements: 1. Regime identification and distant tail variability. *Journal of Geophysical Research*, *103*, 23,503–23,520. <https://doi.org/10.1029/98JA01915>
- Emmert, J. T., Lean, J. L., & Picone, J. M. (2010). Record-low thermospheric density during the 2008 solar minimum. *Geophysical Research Letters*, *37*, L12102. <https://doi.org/10.1029/2010GL043671>
- Emmert, J. T., McDonald, S. E., Drob, D. P., Meier, R. R., Lean, J. L., & Picone, J. M. (2014). Attribution of interminima changes in the global thermosphere and ionosphere. *Journal of Geophysical Research: Space Physics*, *119*, 6657–6688. <https://doi.org/10.1002/2013JA019484>
- Fritz, T. A., Zurbuchen, T. H., Gloeckler, G., Hefti, S., & Chen, J. (2003). The use of iron charge state changes as a tracer for solar wind entry and energization within the magnetosphere. *Annals of Geophysics*, *21*(11), 2155–2164. <https://doi.org/10.5194/angeo-21-2155-2003>
- Fujimoto, M., Terasawa, T., Mukai, T., Saito, Y., Yamamoto, T., & Kokubun, S. (1998). Plasma entry from the flanks of the near-Earth magnetotail: Geotail observations. *Journal of Geophysical Research*, *103*, 4391–4408. <https://doi.org/10.1029/97JA03340>
- Fuselier, S. A., Trattner, K. J., Petrinec, S. M., & Lavraud, B. (2012). Dayside magnetic topology at the Earth's magnetopause for northward IMF. *Journal of Geophysical Research*, *117*, A08235. <https://doi.org/10.1029/2012JA017852>
- Geiss, J., & Young, D. T. (1981). Production and transport of  $O^{++}$  in the ionosphere and plasmasphere. *Journal of Geophysical Research*, *86*, 4739–4750. <https://doi.org/10.1029/JA086iA06p04739>
- Geiss, J., Ogilvie, K. W., von Steiger, R., Mall, U., Gloeckler, G., Galvin, A. B., ... Gliem, F. (1992). Ions with low charges in the solar wind as measured by SWICS on board Ulysses. In E. Marsch, & R. Schwenn (Eds.), *Solar Wind seven (Proc. 3rd COSPAR Colloquium)* (pp. 341–348). Oxford: Pergamon Press. <https://doi.org/10.1016/B978-0-08-042049-3.50074-0>
- Geiss, J., Gloeckler, G., Fisk, L. A., & von Steiger, R. (1995).  $C^+$  pickup ions in the heliosphere and their origin. *Journal of Geophysical Research*, *100*, 23,373–23,377. <https://doi.org/10.1029/95JA03051>
- Gerding, M., Alpers, M., Höffner, J., & von Zahn, U. (2001). Sporadic Ca and  $Ca^+$  layers at mid-latitudes: Simultaneous observations and implications for their formation. *Annals of Geophysics*, *19*, 47–58. <https://doi.org/10.5194/angeo-19-47-2001>
- Gilbert, J. A., Lepri, S. T., Landi, E., & Zurbuchen, T. H. (2012). First measurements of the complete heavy-ion charge state distributions of C, O, and Fe associated with interplanetary coronal mass ejections. *Astronomy Journal*, *751*, 20. <https://doi.org/10.1088/0004-637X/751/1/20>
- Gloeckler, G. (2003). Ubiquitous suprathermal tails on the solar wind and pickup ion distributions. In M. Velli, R. Bruno, & F. Malara (Eds.), *Solar Wind Ten: Proceedings of the Tenth International Solar Wind Conference* (pp. 583–588). New York: American Institute of Physics. <https://doi.org/10.1063/1.1618663>
- Gloeckler, G., & Geiss, J. (1998). Interstellar and inner source pickup ions observed with SWICS on Ulysses. *Space Sci. Rev.*, *86*, 127–159. <https://doi.org/10.1023/A:1005019628054>

- Gloeckler, G., & Geiss, J. (2001). Heliospheric and interstellar phenomena deduced from pickup ion observations. *Space Sci. Rev.*, *97*, 169–181. <https://doi.org/10.1023/A:1011867320416>
- Gloeckler, G., & Hamilton, D. C. (1987). AMPTE ion composition results. *Phys. Scr.*, *T18*, 73–84. <https://doi.org/10.1088/0031-8949/1987/T18/009>
- Gloeckler, G., Wilken, B., Stüdemann, W., Ipavich, F. M., Hovestadt, D., Hamilton, D. C., & Kremser, G. (1985). First composition measurement of the bulk of the storm-time ring current (1 to 300 keV/e) with AMPTE-CCE. *Geophysical Research Letters*, *12*, 325–328. <https://doi.org/10.1029/GL012i005p00325>
- Gloeckler, G., Geiss, J., Balsiger, H., Bedini, P., Cain, J. C., Fischer, J., ... Wilken, B. (1992). The solar wind ion composition spectrometer. *Astronomy & Astrophysics, Supplement Series*, *92*, 267–289.
- Gloeckler, G., Fisk, L. A., Geiss, J., Schwadron, N. A., & Zurbuchen, T. H. (2000). Elemental composition of the inner source pickup ions. *Journal of Geophysical Research*, *105*, 7459–7463. <https://doi.org/10.1029/1999JA000224>
- Gloeckler, G., Fisk, L. A., Zurbuchen, T. H., & Schwadron, N. A. (2000). Sources, injection and acceleration of heliospheric ion populations. In R. Mewaldt, et al. (Eds.), *AIP Conference Proceedings 528: Acceleration and Transport of Energetic Particles Observed in the Heliosphere: ACE 2000 Symposium* (pp. 221–228). New York: American Institute of Physics. <https://doi.org/10.1063/1.1324316>
- Gloeckler, G., Möbius, E., Geiss, J., Bzowski, M., Chalov, S., Fahr, H., ... Zurbuchen, T. (2004). Observations of the helium focusing cone with pickup ions. *Astronomy and Astrophysics*, *426*, 845–854. <https://doi.org/10.1051/0004-6361:20035768>
- Gloeckler, G., Fisk, L. A., & Geiss, J. (2010). Composition of the inner source measured with the solar wind ion composition spectrometer on Ulysses, in Proceeding Solar Wind 12 Conference, Saint-Malo, France, AIP Conference Proceeding, 1216, pp. 514–517, doi<https://doi.org/10.1063/1.3395915>
- Grebowsky, J. M., & Aikin, A. C. (2002). In situ measurements of meteoric ions. In E. Murad, & I. P. Williams (Eds.), *Meteors in the Earth's Atmosphere* (pp. 189–214). Cambridge: Cambridge Univ. Press.
- Grebowsky, J. M., & Aikin, A. C. (2008). Planetary ionospheres—sources and dynamic drivers. *Proc. IAU*, *4(S257)*, 499–510. <https://doi.org/10.1017/S1743921309029780>
- Grebowsky, J. M., Moses, J. I., & Pesnell, W. D. (2002). Meteoric material—An important component of planetary atmospheres. In M. Mendillo, A. Nagy, & J. H. Waite (Eds.), *Atmospheres in the Solar System: Comparative Aeronomy* (pp. 235–244). Washington, DC: American Geophysical Union. <https://doi.org/10.1029/130GM15>
- Grebowsky, J. M., Benna, M., Plane, J. M. C., Collinson, G. A., Mahaffy, P. R., & Jakosky, B. M. (2017). Unique, non-earthlike, meteoritic ion behavior in upper atmosphere of Mars. *Geophysical Research Letters*, *44*, 3066–3072. <https://doi.org/10.1002/2017GL072635>
- Hanson, W. B., Sterling, D. L., & Woodman, R. F. (1972). Source and identification of heavy ions in the equatorial F layer. *Journal of Geophysical Research*, *77*, 5530–5541. <https://doi.org/10.1029/JA077i028p05530>
- Heidrich-Meisner, V., Peleikis, T., Kruse, M., Berger, L., & Wimmer-Schweingruber, R. (2016). Observations of high and low Fe charge states in individual solar wind streams with coronal-hole origin. *Astronomy and Astrophysics*, *593*, A70. <https://doi.org/10.1051/0004-6361/201527998>
- Kallenbach, R., Geiss, J., Gloeckler, G., & von Steiger, R. (2000). Pick-up ion measurements in the heliosphere—A review. *Astrophys. Space Sci.*, *274*, 97. <https://doi.org/10.1023/A:1026587620772>
- Keika, K., Nosé, M., Christon, S. P., & McEntire, R. W. (2004). Acceleration sites of energetic ions upstream of the Earth's bow shock and in the magnetosheath: Statistical study on charge states of heavy ions. *Journal of Geophysical Research*, *109*, A11104. <https://doi.org/10.1029/2003JA009953>
- Keika, K., Nose, M., Ohtani, S.-I., Takahashi, K., Christon, S. P., & McEntire, R. W. (2005). Outflow of energetic ions from the magnetosphere and its contribution to the decay of the storm time ring current. *Journal of Geophysical Research*, *110*, A09210. <https://doi.org/10.1029/2004JA010970>
- Kim, Y. H., Pesnell, W. D., Grebowsky, J. M., & Fox, J. L. (2001). Meteoric i in the ionosphere of Jupiter. *Icarus*, *150*(2), 261–278. <https://doi.org/10.1006/icar.2001.6590>
- Klecker, B., Möbius, E., & Popecki, M. A., (2009). Observation of high ionic charge states of iron at suprathermal energies, in *Proceeding 31th International Cosmic Ray Conference*. Retrieved from <http://icrc2009.uni.lodz.pl/proc/pdf/icrc0278.pdf>
- Ko, Y.-K., Muglach, K., Wang, Y.-M., Young, P. R., & Lepri, S. T. (2014). Temporal evolution of solar wind ion composition and their source coronal holes during the declining phase of cycle 23. I. Low-latitude extension of polar coronal holes. *Astronomy Journal*, *787*, 121. <https://doi.org/10.1088/0004-637X/787/2/121>
- Krimigis, S. M., Mitchell, D. G., Hamilton, D. C., Livi, S., Dandouras, J., Jaskulek, S., ... Williams, D. J. (2004). Magnetosphere Imaging Instrument (MIMI) on the Cassini mission to Saturn/Titan. *Space Science Reviews*, *114*, 233–329. [https://doi.org/10.1007/978-1-4020-2774-1\\_3](https://doi.org/10.1007/978-1-4020-2774-1_3)
- Kronberg, E. A., Bučik, R., Haaland, S., Klecker, B., Keika, K., Desai, M. I., ... Lui, A. T. Y. (2011). On the origin of the energetic ion events measured upstream of the Earth's bow shock by STEREO, Cluster, and Geotail. *Journal of Geophysical Research*, *116*, A02210. <https://doi.org/10.1029/2010JA015561>
- Kumar, S., & Hanson, W. B. (1980). The morphology of metallic ions in the upper atmosphere. *Journal of Geophysical Research*, *85*, 6783–6801. <https://doi.org/10.1029/JA085iA12p06783>
- Le, G., Russell, C. T., & Takahashi, K. (2004). Morphology of the ring current derived from magnetic field observations. *Annals of Geophysics*, *22*(4), 1267–1295. <https://doi.org/10.5194/angeo-22-1267-2004>
- Lepri, S. T., & Zurbuchen, T. H. (2010). Direct observational evidence of filament material within interplanetary coronal mass ejections. *Astronomy Journal Lett.*, *723*, L22–L27. <https://doi.org/10.1088/2041-8205/723/1/L22>
- Lepri, S. T., Zurbuchen, T. H., Fisk, L. A., Richardson, I. G., Cane, H. V., & Gloeckler, G. (2001). Iron charge distribution as an identifier of interplanetary coronal mass ejections. *Journal of Geophysical Research*, *106*, 29,231–29,238. <https://doi.org/10.1029/2001JA000014>
- Liu, L., Zhao, B., Wan, W., Venkartraman, S., Zhang, M.-L., & Yue, X. (2007). Yearly variations of global plasma densities in the topside ionosphere at middle and low latitudes. *Journal of Geophysical Research*, *112*, A07303. <https://doi.org/10.1029/2007JA012283>
- Lockwood, M., Chandler, M. O., Horwitz, J. L., Waite, J. H. Jr., Moore, T. E., & Chappell, C. R. (1985). The cleft ion fountain. *Journal of Geophysical Research*, *90*, 9736–9748. <https://doi.org/10.1029/JA090iA10p09736>
- Mack, C. (1975). *Essentials of Statistics for Scientists and Technologists* (pp. 48). New York: Plenum. [https://doi.org/10.1016/0022-2860\(69\)87020-1](https://doi.org/10.1016/0022-2860(69)87020-1)
- Mall, U. A., Christon, S. P., Kirsch, E., & Gloeckler, G. (2002). On the solar cycle dependence of the N<sup>+</sup>/O<sup>+</sup> content in the magnetosphere and its relation to atomic N and O in the Earth's exosphere. *Geophysical Research Letters*, *29*(12), 1593. <https://doi.org/10.1029/2001GL013957>
- Mann, I., & Czechowski, A. (2005). Dust destruction and ion formation in the inner solar system. *Astronomy Journal*, *621*, L73–L76. <https://doi.org/10.1086/429129>
- Mazur, J. E., Mason, G. M., Looper, M. D., Leske, R. A., & Mewaldt, R. A. (1999). Charge states of solar energetic particles using the geomagnetic cutoff technique: SAMPEX measurements in the 6 November 1997 solar particle event. *Geophysical Research Letters*, *26*, 173–176. <https://doi.org/10.1029/1998GL900075>

- Mazur, J. E., Mason, G. M., Blake, J. B., Klecker, B., Leske, R. A., Looper, M. D., & Mewaldt, R. (2000). Anomalous cosmic ray argon and other rare elements at 1–4 MeV/nucleon trapped within the Earth's magnetosphere. *Journal of Geophysical Research*, *105*, 21,015–21,023. <https://doi.org/10.1029/1999JA000272>
- Mewaldt, R. A., Mason, G. M., Gloeckler, G., Christian, E. R., Cohen, C. M. S., Cummings, A. C., ... Zurbuchen, T. H. (2001). Long-term fluences of energetic particles in the heliosphere. *In AIP Conference Proceedings*, *598*, (p. 165). <https://doi.org/10.1063/1.1433995>
- Möbius, E., Hovestadt, D., Klecker, B., Scholer, M., Gloeckler, G., & Ipavich, F. M. (1985). Direct observation of He<sup>+</sup> pick-up ions of interstellar origin in the solar wind. *Nature*, *318*, 426–429. <https://doi.org/10.1038/318426a0>
- Möbius, E., Hovestadt, D., Klecker, B., Scholer, M., Ipavich, F. M., Carlson, C. W., & Lin, R. P. (1986). A burst of energetic O<sup>+</sup> ions during an upstream particle event. *Geophysical Research Letters*, *13*, 1372–1375. <https://doi.org/10.1029/GL013i013p01372>
- Möbius, E., Popecki, M., Klecker, B., Kistler, L. M., Bogdanov, A., Galvin, B., ... Schmidt, W. K. H. (1999). Energy dependence of the ionic charge state distribution during the November 1997 solar energetic particle event. *Geophysical Research Letters*, *26*, 145–148. <https://doi.org/10.1029/1998GL900131>
- Molina-Cuberos, G. J., López-Moreno, J. J., & Arnold, F. (2008). Meteoric layers in planetary atmospheres. *Space Science Reviews*, *137*, 175–191. <https://doi.org/10.1007/s11214-008-9340-5>
- Nilsson, H., Joko, S., Lundin, R., Rème, H., Sauvaud, J.-A., Dandouras, I., ... Korth, A. (2004). The structure of high altitude O<sup>+</sup> energization and outflow: A case study. *Annals of Geophysics*, *22*, 2497–2506. <https://doi.org/doi:1432-0576/ag/2004-22-2497>
- Nilsson, H., Barghouthi, I. A., Slapak, R., Eriksson, A. I., & André, M. (2012). Hot and cold ion outflow: Spatial distribution of ion heating. *Journal of Geophysical Research*, *117*, A11201. <https://doi.org/10.1029/2012JA017974>
- Nilsson, H., Barghouthi, I. A., Slapak, R., Eriksson, A. I., & André, M. (2013). Hot and cold ion outflow: Observations and implications for numerical models. *Journal of Geophysical Research: Space Physics*, *118*, 105–117. <https://doi.org/10.1029/2012JA017975>
- Nishida, A. (1994). Foreword by GEOTAIL program manager. *Journal of Geomagnetism and Geoelectricity*, *46*, 3–5. <https://doi.org/10.5636/jgg.46.3>
- Nishida, A., & Mukai, T. (2015). ISAS-NASA GEOTAIL Satellite. In J. N. Pelton, & F. Allahdadi (Eds.), *Handbook of Cosmic Hazards and Planetary Defense (Springer Reference Work 2015)* (pp. 371–397). Switzerland: Springer. [https://doi.org/10.1007/978-3-319-03952-7\\_27](https://doi.org/10.1007/978-3-319-03952-7_27)
- Nosé, M., Ieda, A., & Christon, S. P. (2009). Geotail observations of plasma sheet ion composition over 16 years: On variations of average plasma ion mass and O<sup>+</sup> triggering substorm model. *Journal of Geophysical Research*, *114*, A07223. <https://doi.org/10.1029/2009JA014203>
- Ogawa, Y., Buchert, S. C., Sakurai, A., Nozawa, S., & Fujii, R. (2010). Solar activity dependence of ion upflow in the polar ionosphere observed with the European Incoherent Scatter (EISCAT) Tromsø UHF radar. *Journal of Geophysical Research*, *115*, A07310. <https://doi.org/10.1029/2009JA014766>
- Oka, M., Terasawa, T., Noda, H., Saito, Y., & Mukai, T. (2002). Acceleration of interstellar helium pickup ions at the Earth's bow shock: GEOTAIL observation. *Geophysical Research Letters*, *29*(14), 1688. <https://doi.org/10.1029/2001GL014150>
- Ono, Y., Nosé, M., Christon, S. P., & Lui, A. T. Y. (2009). The role of magnetic field fluctuations in nonadiabatic acceleration of ions during dipolarization. *Journal of Geophysical Research*, *114*, A05209. <https://doi.org/10.1029/2008JA013918>
- Pesnell, W. D., & Grebowsky, J. M. (2001). Meteoric ions in planetary ionospheres. *Advances in Space Research*, *27*(11), 1807–1814. [https://doi.org/10.1016/S0273-1177\(01\)00264-2](https://doi.org/10.1016/S0273-1177(01)00264-2)
- Peterson, W. K., Abe, T., Fukunishi, F., Greffen, M. J., Hayakawa, H., ... Yau, A. W. (1994). On the sources of energization of molecular ions at ionospheric altitudes. *Journal of Geophysical Research*, *99*, 23,257–23,274. <https://doi.org/10.1029/94JA01738>
- Plane, J. M. C. (2012). Cosmic dust in the Earth's atmosphere (Critical Review). *Chemical Society Reviews*, *41*, 6507–6518. <https://doi.org/10.1039/C2CS35132C>
- Plane, J. M. C., Feng, W., & Dawkins, E. C. M. (2015). The mesosphere and metals: Chemistry and Changes. *Chemical Reviews*, *2015*(115), 4497–4541. <https://doi.org/10.1021/cr500501>
- Plane, J. M. C., Gómez-Martín, J. C., Feng, W., & Janches, D. (2016). Silicon chemistry in the mesosphere and lower thermosphere. *Journal of Geophysical Research Atmos.*, *121*, 3718–3728. <https://doi.org/10.1002/2015JD024691>
- Posner, A., Schwadron, N. A., Zurbuchen, T. H., Kozyra, J. U., Liemohn, M. W., & Gloeckler, G. (2002). Association of low-charge-state heavy ions up to 200 R<sub>E</sub> upstream of the Earth's bow shock with geomagnetic disturbances. *Geophysical Research Letters*, *29*(7), 1099. <https://doi.org/10.1029/2001GL013449>
- Rubin, A. E., & Grossman, J. N. (2010). Meteorite and meteoroid: New comprehensive definitions. *Meteoritics and Planetary Science*, *45*(1), 114–122. <https://doi.org/10.1111/j.1945-5100.2009.01009.x>
- Schwadron, N. A., Combi, M., Huebner, W., & McComas D. J. (2002). The outer source of pickup ions and anomalous cosmic rays. *Geophysical Research Letters*, *29*(20), 1993. <https://doi.org/10.1029/2002GL015829>
- Smyth, W. H., & Marconi, M. L. (2003). Nature of the iogenic plasma source in Jupiter's magnetosphere I. Circumplanetary distribution. *Icarus*, *166*, 85–106. [https://doi.org/10.1016/S0019-1035\(03\)00176-3](https://doi.org/10.1016/S0019-1035(03)00176-3)
- Spjeldvik, W. N. (1979). Expected charge states of energetic ions in the magnetosphere. *Space Science Reviews*, *23*(3), 499–538. <https://doi.org/10.1007/BF00172252>
- Spjeldvik, W. N. (1996). Numerical modeling of stably and transiently confined energetic heavy ion radiation in the Earth's magnetosphere. *Radiation Measurements*, *26*(3), 309–320. [https://doi.org/10.1016/1350-4487\(96\)00059-5](https://doi.org/10.1016/1350-4487(96)00059-5)
- Spjeldvik, W. N., Bourdarie, S., & Boschen, D. (2002). Solar origin iron ions in the Earth's radiation belts: Multi-dimensional equilibrium configuration modeling with charge states 1 through 12. *Advances in Space Research*, *30*(12), 2835–2838. [https://doi.org/10.1016/S0273-1177\(02\)80426-4](https://doi.org/10.1016/S0273-1177(02)80426-4)
- Taut, A., Berger, L., Drews, C., & Wimmer-Schweingruber, R. F. (2015). Composition of inner-source heavy pickup ions at 1 AU: SOHO/CELIAS/CTOF observations—Implications for the production mechanisms. *Astronomy and Astrophysics*, *576*(A55), 2015. <https://doi.org/10.1051/0004-6361/201425139>
- Terasawa, T., Fujimoto, M., Mukai, T., Shinohara, I., Saito, Y., Yamamoto, T., ... Lepping, R. P. (1997). Solar wind control of density and temperature in the near-Earth plasma sheet: WIND/GEOTAIL collaboration. *Geophysical Research Letters*, *24*, 935–938. <https://doi.org/10.1029/96GL04018>
- Thayer, J. P. (1998). Height-resolved joule heating rates in the high-latitude E region and the influence of neutral winds. *Journal of Geophysical Research*, *103*, 471–487. <https://doi.org/10.1029/97JA02536>
- Trattner, K. J., Burch, J. L., Ergun, R., Fuselier, S. A., Gomez, R. G., Grimes, E. W., ... Young, D. T. (2016). The responsetime of the magnetopause reconnection location to changes in the solar wind: MMS case study. *Geophysical Research Letters*, *43*, 4673–4682. <https://doi.org/10.1002/2016GL068554>

- von Steiger, R., Schwadron, N. A., Fisk, L. A., Geiss, J., Gloeckler, G., Hefti, S., ... Zurbuchen, T. H. (2000). Composition of quasi-stationary solar wind flows from Ulysses/Solar Wind Ion Composition Spectrometer. *Journal of Geophysical Research*, *105*, 27,217–27,238. <https://doi.org/10.1029/1999JA000358>
- Westlake, J. H., Cohen, I. J., Mauk, B. H., Anderson, B. J., Mitchell, D. G., Gkioulidou, M., ... Russell, C. T. (2016). The permeability of the magnetopause to a multispecies substorm injection of energetic particles. *Geophysical Research Letters*, *43*, 9453–9460. <https://doi.org/10.1002/2016GL070189>
- Wicks, R. T., Owens, M. J., & Horbury, T. S. (2010). The variation of solar wind correlation lengths over three solar cycles. *Solar Physics*, *262*(1), 191–198. <https://doi.org/10.1007/s11207-010-9509-4>
- Williams, D. J., McEntire, R. W., Schlemm, C. II, Lui, A. T. Y., Gloeckler, G., Christon, S. P., & Gliem, F. (1994). Geotail energetic particles and ion composition instrument. *Journal of Geomagnetism and Geoelectricity*, *46*, 39–57. <https://doi.org/10.5636/jgg.46.39>
- Wimmer-Schweingruber, R. F. & Bochsler, P. (2003). On the origin of inner-source pickup ions. *Geophysical Research Letters*, *30*(2), 1077. <https://doi.org/10.1029/2002GL015218>
- Zoennchen, J. H., Nass, U., & Fahr, H. J. (2015). Terrestrial exospheric hydrogen density distributions under solar minimum and solar maximum conditions observed by the TWINS stereo mission. *Annals of Geophysics*, *33*, 413–426. <https://doi.org/10.5194/angeo-33-413-2015>